DISSERTATION

Multi-Timescale Dynamics using High-Repetition-Rate Single-Shot Spectroscopy

高繰り返しシングルショット法による マルチ時間スケールダイナミクスの研究

Masataka Kobayashi

March 2021

Advisor
Professor Ikufumi Katayama

Graduate School of Engineering Science
Yokohama National University

Abstract

High-density photoexcitation using laser pulses can induce drastic changes in the electronic states and atomic arrangements of materials, leading to cooperative phenomena such as photoinduced phase change, surface modification, and laser ablation. These phenomena are irreversible reactions triggered by fast sub-picosecond-scale relaxation dynamics associated with electronic excitation, resulting in the formation of nuclei and domains and structural changes occurring from nanosecond to microsecond timescales. Thus, observation of pulse-to-pulse ultrafast dynamics is key to understanding multi-timescale phenomena.

In recent years, several schemes for single-shot spectroscopy that enables us to capture an entire ultrafast signal waveform in a single probe shot have been proposed, and these techniques made it possible to measure photoinduced irreversible phenomena. However, these single-shot techniques rely on two-dimensional (2D) detectors, such as charge-coupled devices (CCDs) or complementary metal-oxide-semiconductor (CMOS) cameras, which limit the readout speed of the pump-probe traces at a high repetition rate and hinder real-time visualization and manipulation of signal waveforms. Therefore, conventional single-shot spectroscopy cannot capture pulse-to-pulse transitions in multi-timescale dynamics.

In this thesis, we propose a novel scheme for high-repetition-rate single-shot spectroscopy, which combines time encoding with a photonic time-stretching technique. Since this scheme uses only a single photodiode and an oscilloscope for data readout, it enables us to readily detect a complete dataset composed of multiple pump-probe traces with microsecond time intervals. This thesis is organized as follows:

- First, we demonstrated the high-repetition single-shot method using a long optical fiber, a photodiode, and an oscilloscope. By measuring the intensity dependence of the optical Kerr signals within one second, we showed the potential of our single-shot method.

- Second, we improved the sensitivity and variable time window of the high-repetition single-shot method using a chirped fiber Bragg grating (CFBG) and grating pair.
- Finally, using our method, we investigated the pulse-to-pulse ultrafast dynamics at each step in a series of photoinduced irreversible events, the photoinduced phase change from the crystalline phase to the amorphous phase, and the subsequent pulse-to-pulse laser-induced periodic surface structure (LIPSS) formation in $Ge_2Sb_2Te_5$ (GST) films. We found that pump-probe relaxation time and amplitude during LIPSS formation decreases with an increase in pump laser shots.

These results could contribute to the observation of pulse-to-pulse dynamics. In addition, the observation of ultrafast dynamics at each pulse is important in many fields, such as laser chaos, optical solitons, and biotechnology. In addition, our multi-shot ultrafast dynamics measurement method could be useful for understanding fundamental processes in various other irreversible phenomena in the future.

Acknowledgements

First, I would like to express my deepest gratitude to my supervisor, Professor Ikufumi Katayama, for his help during my studies. I could not have written this thesis without his insightful and broad-minded advice. He also helped me improve my writing and speaking skills and taught me physics, no matter how busy he was.

Secondly, I would like to thank my co-supervisor, Professor Jun Takeda for his continuous support and discussions based on his extensive scientific knowledge. His advice led me to evaluate my research topic and decide on my research direction.

I would like to thank the academic community for supporting my research. Professor Jeremy A. Johnson, a former Visiting Professor at the laboratory and now a Professor at Brigham Young University (BYU), helped me to construct the experimental setup. He also supported my studies at BYU. Dr. Yasuo Minami, a former Assistant Professor at the laboratory and now an Associate Professor at Tokushima University, taught me how to operate and adjust the femtosecond laser system. Dr. Yusuke Arashida, a former Assistant Professor at the laboratory and now an Assistant Professor at the University of Tsukuba, brought his extensive knowledge of physics to our discussions. Dr. Kanta Asakawa, a former Assistant Professor at the laboratory and now an Assistant Professor at Tokyo University of Agriculture and Technology, shared his knowledge of surface physics and Japanese Kendama techniques. Dr. Keisuke Kaneshima, who worked as an Assistant Professor at the laboratory, for many helpful discussions and advice.

I would like to express my gratitude to many people outside the laboratory. Professor Masaaki Ashida at Osaka University provided access to experimental facilities. I wish to thank Professor Junji Yumoto and Assistant Professor Kuniaki Konishi at the University of Tokyo for insightful discussions and teaching me laser processing. I also thank Dr. Isao Morohashi at the National Institute of Information and Communications Technology (NICT) for fruitful discussions about the high-repetition-rate single-shot detection system.

The studies presented in this thesis were supported by the cooperation of many members of the Takeda and Katayama laboratories. It has been my great pleasure to work and study with them for the past six years. I would like to thank Mr. Yuhei

Miyamoto, Mr. Kohei Kawana, and Mr. Ken-ichi Izumi for their company during the development of high-repetition-rate single-shot measurements with a CFBG.

Finally, I would like to express my gratitude to my family and friends for their endless support. Especially, I could not have completed this work without the support of my parents. I thank them from the bottom of my heart for allowing me to explore science.

Yokohama
February 2021

Masataka Kobayashi

Contents

Chapter 1

Introduction and Background

1.1 Multi-Timescale Phenomena

High-density photoexcitation using laser pulses can induce drastic changes in the electronic states and atomic arrangements of materials, which leads to cooperative phenomena such as photoinduced phase changes [1-4], surface modification, and laser ablation [5-10]. These phenomena are irreversible reactions that are triggered by fast sub-picosecond-scale relaxation dynamics associated with electronic excitation, resulting in the formation of nuclei and domains and in structural changes on a wide range of timescales (from nanosecond to microsecond). The energy input during photoexcitation is extremely large, extending to a timescale

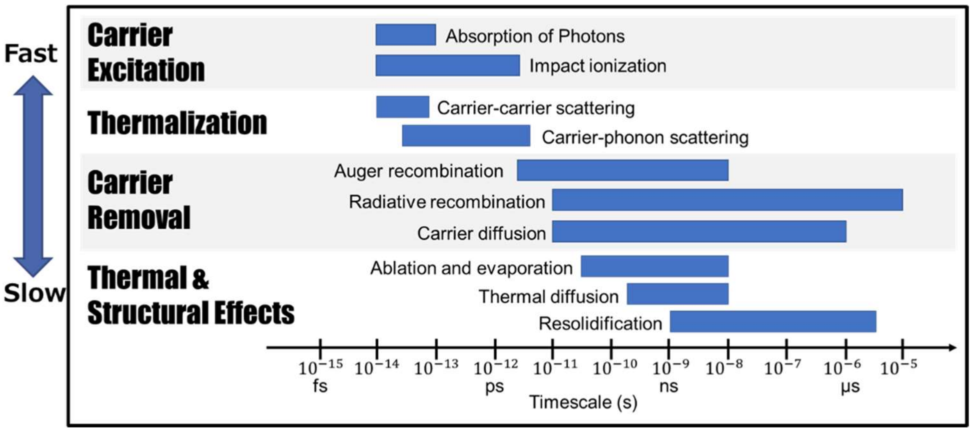

Figure 1.1 | Examples of the timescales of photoinduced phenomena using intense laser pulses. Adapted from Ref. [11].

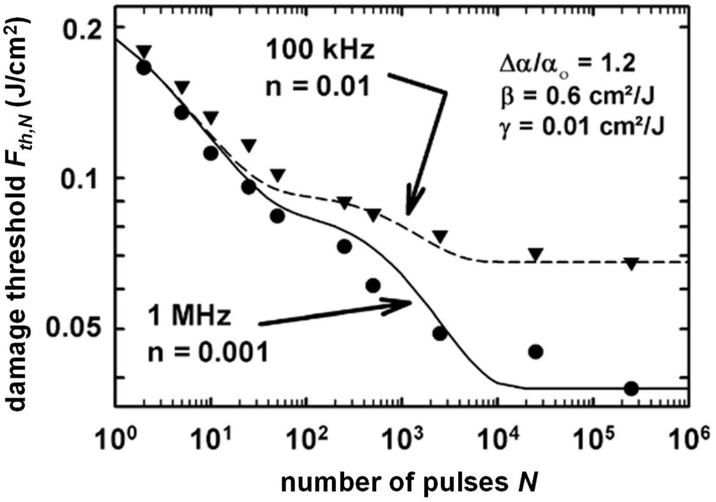

Figure 1.2 | Incubation effect in laser processing. Laser damage (ablation) threshold fluence as a function of number of pulses for stainless steel at two laser repetition rates. Adapted from Ref. [14].

of several orders of magnitude [11]. Figure 1.1 shows examples of the timescales of photoinduced phenomena using intense laser pulses. Such a multi-timescale nature of these phenomena often lead to distinct results obtained from single and multiple excitations, such as the incubation effect in laser processing [12-15] and the formation of laser-induced periodic surface structures (LIPSS) [5,16-19]. Thus, observing pulse-to-pulse ultrafast dynamics is key for understanding multi-timescale phenomena occurring under high-density excitation. Additionally, initial relaxation processes determine how the input energy is distributed in materials after photoexcitation. Understanding this mechanism is important not only for physics but also for applications such as material control and laser manufacturing. Therefore, experimental tools to investigate changes in their ultrafast pulse-to-pulse dynamics are strongly desired.

Pump-probe spectroscopy, or sampling spectroscopy, is a well-known method to obtain picosecond or femtosecond dynamics information [20,21]. Figure 1.3 shows a typical experiment setup for pump-probe spectroscopy using laser pulses. By controlling the delay time between the pump and probe pulses using a delay stage, the ultrafast response of pump pulse-induced changes, such as optical constants and permittivity, is detected by the intensity modulation of the probe pulse. However, conventional pump-probe spectroscopy normally assumes the repetition

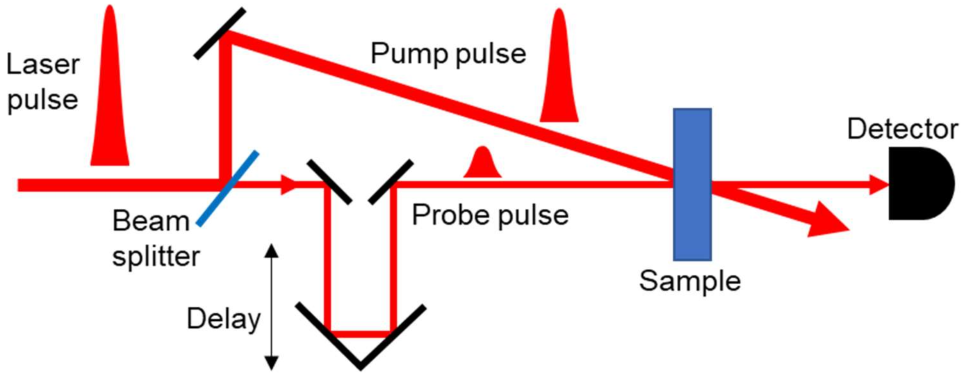

Figure 1.3 | Typical experimental setup for conventional pump-probe spectroscopy.

of the same phenomena during the measurements of pump-probe signals at different delay times, limiting its applicability to reversible phenomena. Therefore, it is difficult to investigate dynamics of irreversible phenomena and pulse-to-pulse dynamics using conventional methods.

1.2 Single-Shot Spectroscopy

To overcome the difficulty of conventional pump-probe spectroscopy, several schemes for single-shot spectroscopy that enable capture of an entire ultrafast signal

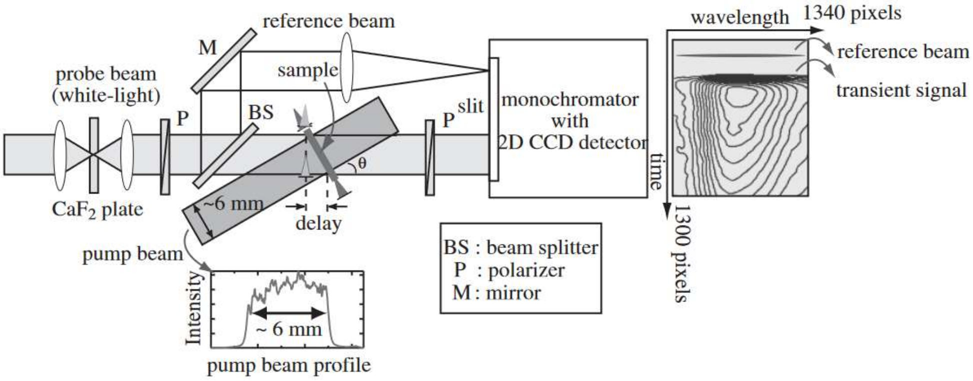

Figure 1.4 | Experimental setup for real-time pump-probe imaging spectroscopy [27]. Adapted from Ref. [27].

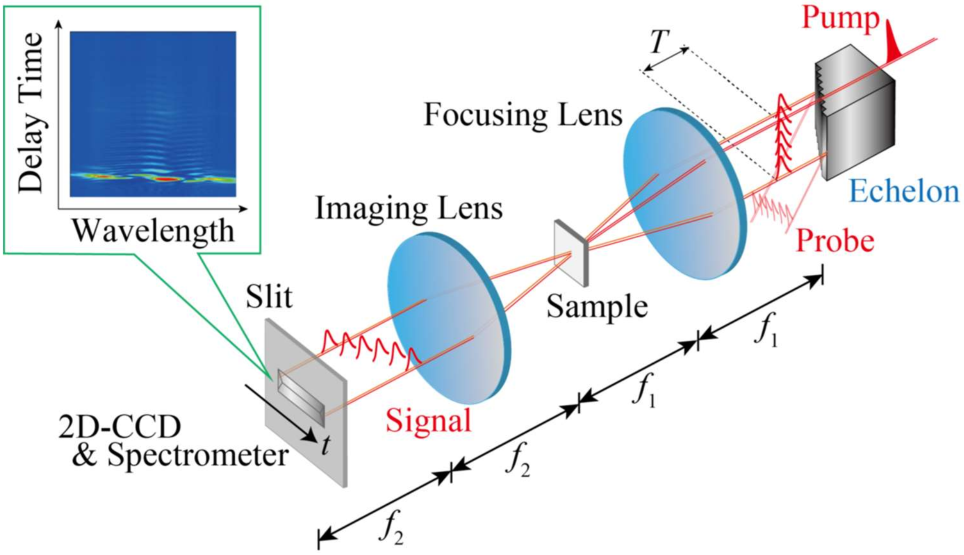

Figure 1.5 | Experimental setup for single-shot time-frequency imaging spectroscopy using a reflection echelon mirror [33]. Adapted from Ref. [33].

waveform in a single probe shot have been proposed in recent years. Examples of such schemes include the chirped-pulse time-encoding method [22-24], the real-time imaging method [25-27], and echelon-based methods [28-33]. The ultrafast response induced by the pump pulse can be measured in a single shot by modifying the probe pulse via chirping, inclining, or dividing into daughter pulses. These single-shot techniques have enabled measurement of various interesting phenomena, from photoinduced irreversible [29,34] and asynchronous, or chaotic, [35,36] to picosecond shot-to-shot jitter-related phenomena [37,38].

However, these single-shot techniques rely on 2D detectors, such as charge-coupled devices (CCDs) or complementary metal-oxide-semiconductor (CMOS) cameras, to detect the waveform. This limits the readout speed of pump-probe traces at a high-repetition-rate and hinders real-time visualization and manipulation of signal waveforms. Additionally, a high-frame-rate 2D detector offers limited temporal (or spatial) resolution due to the trade-off between frame rate and resolution. Therefore, conventional single-shot spectroscopy has revealed only the initial processes of photoinduced phenomena and has failed to capture real-time pulse-to-pulse transitions. For a single-shot measurement of pulse-to-pulse ultrafast dynamics at timescales ranging from nanosecond to microsecond, it is necessary to increase the acquisition rate without using 2D detectors.

1.3 Photonic Time-Stretch Method

The photonic time-stretch method is a high-repetition-rate spectrum measurement method comprised of an optical fiber and an oscilloscope. This method was reported by the Jalali group in 1998 [39,40]. Using a sampling oscilloscope, high-frequency electrical signals could be stretched in time and down-converted using chirped optical pulses and dispersion in optical fibers [41]. Improvements and wide-banding in measurement instruments, especially photodetectors and real-time oscilloscopes, made it possible to read out the time-stretched signal faster. This was shown by the Goda and Jalali groups in 2009, who reported a serial time-encoded imaging system using the photonic time-stretch method [42]. Despite its simplicity, the imaging system achieved frame rates more than 1,000 times faster than those of conventional 2D imaging methods using CCDs. Consequently, the photonic time-stretch method has been investigated for many applications [43], such as label-free noncontact bioimaging [44], ultrafast structural imaging [45], electron bunch evaluation in accelerators [46], mode-locking in pulsed lasers [47], and optical soliton production processes [48].

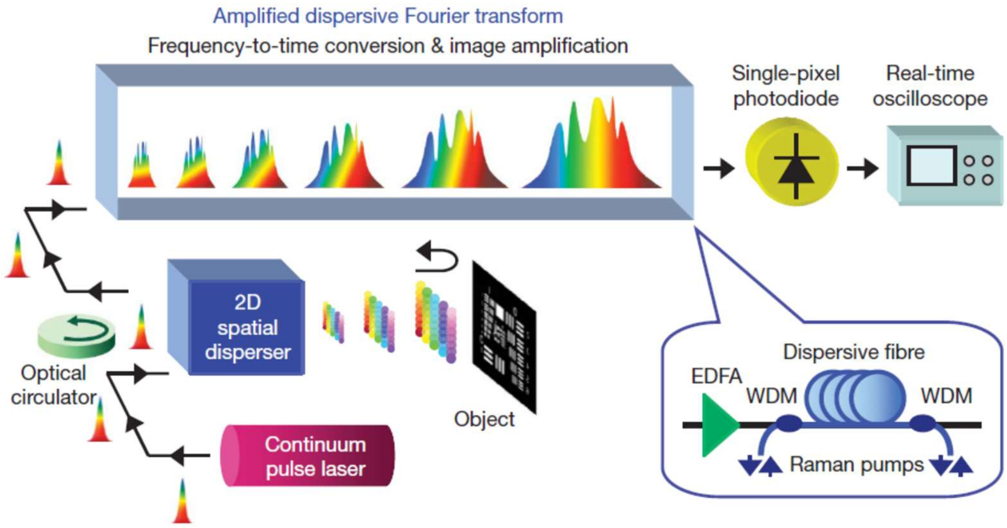

Figure 1.5 | Schematic of serial time-encoded amplified imaging. Adapted from Ref. [39].

Such a high-frame-rate spectral measurement technique is currently being studied for various applications; however, few examples have combined the photonic time-stretch method with single-shot pump-probe spectroscopy to demonstrate its potential.

1.4 Thesis Purpose

In this thesis, we demonstrate a new method to measure ultrafast dynamics with a high-repetition-rate [49,50]. A chirped laser pulse was used to map femtosecond time information onto the spectrum of the probe pulse [22-24] and, instead of using a spectrometer and a CCD or CMOS camera, an optical time-stretching method with an optical fiber was used to obtain modulated probe spectrum as a nanosecond temporal modulation of the intensity profile [39-42]. Because the nanosecond temporal modulation can be measured using a single photodiode and an oscilloscope, we were able to realize high-repetition-rate single-shot measurements of ultrafast dynamics. This measurement is only limited by the repetition rate of the laser system and the acquisition rate of the recording oscilloscope. Therefore, the following observations can be performed using this method: the dynamics of long relaxation times with high time resolution and the accumulation effect of multi-pulse excitation, pulse-by-pulse. In this thesis, we will focus on the latter observation.

The purpose of this study was to develop and demonstrate a high-repetition-rate single-shot spectroscopy method and, by continuously measuring irreversible photoinduced phase change and surface modification phenomena over a wide range of timescales, we aimed to shed light on the link between femtosecond-to-picosecond ultrafast dynamics processes and microsecond to millisecond structural changes.

1.5 Thesis Organization

In Chapter 2, the nature of the chirped pulse and group delay dispersion is described. Then, the chirped pulse single-shot method and the theory of the photonic time-stretch method are explained. Finally, the concept of the experimental setup is introduced.

In Chapter 3, the results of our high-repetition single-shot method, using a long optical fiber, a photodiode, and an oscilloscope, are described. The intensity dependence of optical Kerr signals within one second is demonstrated and the superiority of our single-shot method over conventional approaches is discussed.

In Chapter 4, improvements in the sensitivity and variable time window of our high-repetition single-shot method are demonstrated using a chirped fiber Bragg grating (CFBG) and grating pair.

In Chapter 5, using high-repetition-rate single-shot spectroscopy with a CFBG, pulse-to-pulse ultrafast dynamics in a series of photoinduced irreversible events, such as the photoinduced phase change from crystalline-to-amorphous phase and subsequent LIPSS formation in $Ge_2Sb_2Te_5$ (GST) films, are shown.

Finally, in Chapter 6, a summary of our results is provided and further research opportunities and developments are discussed.

References

[1] S. Koshihara, Y. Tokura, K. Takeda, and T. Koda, "Reversible photoinduced phase transitions in single crystals of polydiacetylenes," Phys. Rev. Lett. **68,** 1148 (1992).

[2] T. Tayagaki, and K. Tanaka, "Photoinduced phase transition to a new macroscopic spin-crossover-complex phase," Phys. Rev. Lett. **86,** 2886 (2001).

[3] T. Taniguchi, H. Sato, Y. Hagiwara, T. Asahi, and H. Koshima, "Photo-triggered phase transition of a crystal," Commun. Chem. **2,** 19 (2019).

[4] M. Hada, W. Oba, M. Kuwahara, I. Katayama, T. Saiki, J. Takeda, K. G. Nakamura, "Ultrafast time-resolved electron diffraction revealing the nonthermal dynamics of near-UV photoexcitation-induced amorphization in $Ge_2Sb_2Te_5$," Sci. Rep. **5**, 13530 (2015).

[5] M. Birnbaum, "Semiconductor surface damage produced by ruby lasers," J. Appl. Phys. **36,** 3688 (1965).

[6] Z. Guosheng, P. M. Fauchet, and A. E. Siegman, "Growth of spontaneous periodic surface structures on solids during laser illumination," Phys. Rev. B **26**, 5366 (1982).

[7] C. Momma, B. N. Chichkov, S. Nolte, F. Von Alvensleben, A. Tünnermann, H. Welling, and B. Wellegehausen, "Short-pulse laser ablation of solid targets," Opt. Commun. **129**, 134 (1996).

[8] G. Dumitru, V. Romano, H. Weber, M. Sentis and W. Marine, "Femtosecond ablation of ultrahard materials," Appl. Phys. A **74**, 729 (2002).

[9] K. Sugioka, "Progress in ultrafast laser processing and future prospects," Nanophotonics **6**, 393 (2017).

[10] M. Beresna, M. Gecevičius, P. G. Kazansky, and T. Gertus, "Radially polarized optical vortex converter created by femtosecond laser nanostructuring of glass," Appl. Phys. Lett. **98**, 1 (2011).

[11] K. C. Phillips, H. H. Gandhi, E. Mazur, and S. K. Sundaram, "Ultrafast laser processing of materials: a review," Adv. Opt. Photon. **7,** 684-712 (2015).

[12] M. Lenzner, J. Krüger, W. Kautek, and F. Krausz, "Incubation of laser ablation in fused silica with 5-fs pulses," Appl. Phys. A **69**, 465 (1999).

[13] A. Rosenfeld, M. Lorenz, R. Stoian, and D. Ashkenasi, "Ultrashort-laser-pulse damage threshold of transparent materials and the role of incubation," Appl. Phys. A **69**, S373 (1999).

[14] Z. Sun, M. Lenzner, and W. Rudolph, "Generic incubation law for laser damage and ablation thresholds," J. Appl. Phys. **117**, 073102 (2015).

[15] H. Sakurai, C. He, K. Konishi, H. Tamaru, J. Yumoto, M. Kuwata-Gonokami and A. Gillner, "Effect of damage incubation in the laser grooving of sapphire," J. Appl. Phys. **125**, 173109 (2019).

[16] Jeff F. Young, J. E. Sipe, and H. M. van Driel, "Laser-induced periodic surface structure. III. Fluence regimes, the role of feedback, and details of the induced topography in germanium," Phys. Rev. B **30,** 2001 (1984).

[17] D. Ashkenasi, A. Rosenfeld, H. Varel, M. Wahmer, and E. E. B. Campbell, "Subwavelength ripple formation on the surfaces of compound semiconductors irradiated with femtosecond laser pulses," Appl. Surf. Sci. **120**, 65 (1997).

[18] S. Sakabe, M. Hashida, S. Tokita, S. Namba, and K. Okamuro, "Mechanism for self-formation of periodic grating structures on a metal surface by a femtosecond laser pulse," Phys. Rev. B **79,** 033409-1 (2009).

[19] J. Bonse, J. Krüger, S. Höhm and A. Rosenfeld, "Femtosecond laser-induced periodic surface structures," J. Laser Appl. **24,** 4 (2012).

[20] N. Furukawa, and J. Takeda, "Ultrafast internal conversion of all-trans-β-carotene studied by femtosecond spectroscopy," Nonlinear Optics, **29**, 579 (2002).

[21] J.-P. Zhang, L. H. Skibsted, R. Fujii, and Y. Koyama, "Transient absorption from the $1B_u^+$ state of all-trans-β-carotene newly identified in the near-infrared region," Photochem. Photobiol. **73**, 219 (2001).

[22] K. Y. Kim, B. Yellampalle, G. Rodriguez, R. D. Averitt, A. J. Taylor, and J. H. Glownia, "Single-shot, interferometric, high-resolution, terahertz field diagnostic," App. Phys. Lett. **88**, 041123 (2006).

[23] B. Yellampalle, K. Y. Kim, G. Rodriguez, J. H. Glownia, and A. J. Taylor, "Algorithm for high-resolution single-shot THz measurement using in-line spectral interferometry with chirped pulses," App. Phys. Lett. **87**, 211109 (2005).

[24] J.-P. Geindre, P. Audebert, S. Rebibo, and J.-C. Gauthier, "Single-shot spectral interferometry with chirped pulses," Opt. Lett. 26, 1612 (2001).

[25] L. Dhar, J. T. Fourkas, and K. A. Nelson, "Pulse-length-limited ultrafast pump–probe spectroscopy in a single laser shot," Opt. Lett. **19**, 643 (1994).

[26] N. Furukawa, C. E. Mair, V. D. Kleiman, and J. Takeda, "Femtosecond real-time pump-probe imaging spectroscopy," Appl. Phys. Lett. **85,** 4645 (2004).

[27] Y. Makishima, N. Furukawa, A. Ishida, and J. Takeda, "Femtosecond real-time pump-probe imaging spectroscopy implemented on a single shot basis," Jpn. J. Appl. Phys. **45,** 1 (2006).

[28] G. P. Wakeham, and K. A. Nelson, "Dual-echelon single-shot femtosecond spectroscopy," Opt. Lett. **25,** 505 (2000).

[29] Y. Minami, Y. Hayashi, J. Takeda, and I. Katayama, "Single-shot measurement of a terahertz electric-field waveform using a reflective echelon mirror," Appl. Phys. Lett. **103,** 051103 (2013).

[30] H. Sakaibara, Y. Ikegaya, I. Katayama, and J. Takeda, "Single-shot time-frequency imaging spectroscopy using an echelon mirror," Opt. Lett. **37,** 1118 (2012).

[31] I. Katayama, H. Sakaibara, and J. Takeda, "Real-time time-frequency imaging of ultrashort laser pulses using an echelon mirror," Jpn. J. Appl. Phys., Part 1 **50,** 102701 (2011).

[32] T. Kuribayashi, T. Motoyama, Y. Arashida, I. Katayama, and J. Takeda, "Anharmonic phonon-polariton dynamics in ferroelectric $LiNbO_3$ studied with single-shot pump-probe imaging spectroscopy," J. Appl. Phys. **123,** 174103 (2018).

[33] T. Kuribayashi, "Dynamics of ferroelectric phonon-polariton wavepackets propagation and quantum control," Yokohama National Univ., Master's thesis (2015).

[34] J. Takeda, W. Oba, Y. Minami, T. Saiki, and I. Katayama, "Ultrafast crystalline-to-amorphous phase transition in $Ge_2Sb_2Te_5$ chalcogenide

alloy thin film using single-shot imaging spectroscopy," Appl. Phys. Lett. **104,** 261903 (2014).

[35] J. van Tilborg, C. Tóth, N. H. Matlis, G. R. Plateau, and W. P. Leemans, "Single-shot measurement of the spectral envelope of broad-bandwidth terahertz pulses from femtosecond electron bunches," Opt. Lett. **33,** 1186 (2008).

[36] I. Wilke, A. M. MacLeod, W. A. Gillespie, G. Berden, G. M. H. Knippels, and A. F. G. van der Meer, "Single-Shot Electron-Beam Bunch Length Measurements," Phys. Rev. Lett., **88,** 124801 (2002).

[37] M. Beye, O. Krupin, G. Hays, A. H. Reid, D. Rupp, S. de Jong, S. Lee, W.-S. Lee, Y.-D. Chuang, R. Coffee, J. P. Cryan, J. M. Glownia, A. Föhlisch, M. R. Holmes, A. R. Fry, W. E. White, C. Bostedt, A. O. Scherz, H. A. Durr, and W. F. Schlotter, "X-ray pulse preserving single-shot optical cross-correlation method for improved experimental temporal resolution," Appl. Phys. Lett. **100,** 121108 (2012).

[38] M. Harmand, R. Coffee, M. R. Bionta, M. Chollet, D. French, D. Zhu, D. M. Fritz, H. T. Lemke, N. Medvedev, B. Ziaja, S. Toleikis, and M. Cammarata, "Achieving few-femtosecond time-sorting at hard X-ray free-electron lasers," Nat. Photon. **7,** 215 (2013).

[39] A. S. Bhushan, F. Coppinger, and B. Jalali, "Time-stretched analog-to-digital conversion," Electron. Lett. **34,** 9, 839 (1998).

[40] F. Coppinger, A. S. Bhushan, and B. Jalali, "Time magnification of electrical signals using chirped optical pulses," Electron. Lett. **34,** 4, 399 (1998).

[41] F. Coppinger, A. S. Bhushan, and B. Jalali, "Photonic time stretch and its application to analog-to-digital conversion," IEEE Transactions on microwave theory and techniques **47,** 7 (1999).

[42] K. Goda, K. K. Tsia and B. Jalali, "Serial time-encoded amplified imaging for real-time observation of fast dynamic phenomena," Nature 458, 7242, 1145 (2009).

[43] A. Mahjoubfar, D. V Churkin, S. Barland, N. Broderick, S.K. Turitsyn, and B. Jalali, "Time stretch and its applications," Nat. Photonics **11**, 341 (2017).

[44] B. Jalali, P. Soon-Shiong, and K. Goda, “Breaking speed and sensitivity limits: real-time diagnostics with serial time-encoded amplified microscopy,” Optik Photonik **5,** 32 (2010).

[45] J. L. Wu, Y. Q. Xu, J. J. Xu, X. M. Wei, A. C. S Chan, A. H. L Tang, A. K. S Lau, B. M. F Chung, H. C. Shum, E. Y Lam, K. K. Y Wong, and K. K. Tsia, “Ultrafast laser-scanning time-stretch imaging at visible wavelengths,” Light Sci. Appl. **6,** e16196 (2017).

[46] E. Roussel, C. Evain, M. Le Parquier, C. Szwaj, S. Bielawski, L. Manceron, J.-B. Brubach, M.-A. Tordeux, J.-P. Ricaud, L. Cassinari, M. Labat, M.-E Couprie, and P. Roy, “Observing microscopic structures of a relativistic object using a time-stretch strategy,” Sci. Rep. **5,** 10330 (2015).

[47] G. Herink, B. Jalali, C. Ropers, and D.R. Solli, “Resolving the build-up of femtosecond mode-locking with single-shot spectroscopy at 90 MHz frame rate,” Nat. Photonics **10**, 321 (2016).

[48] G. Herink, F. Kurtz, B. Jalali, D. R. Solli, and C. Ropers, “Real-time spectral interferometry probes the internal dynamics of femtosecond soliton molecules,” Science **356,** 50 (2017).

[49] M. Kobayashi, Y. Minami, C. L. Johnson, P. D. Salmans, N. R. Ellsworth, J. Takeda, J. A. Johnson and I. Katayama, “High-acquisition-rate single-shot pump-probe measurements using time-stretching method,” Sci. Rep. **6,** 37614 (2016).

[50] M. Kobayashi, Y. Arashida, G. Yamashita, E. Matsubara, M. Ashida, J. A. Johnson, and I. Katayama, “Fast-frame single-shot pump-probe spectroscopy with chirped-fiber-Bragg gratings,” Opt. Lett. **44,** 163 (2019).

Chapter 2

Experimental Methods & Concepts

In this chapter, the experimental methods and concepts relevant to this thesis are introduced. The concept of a chirped pulse is important because many of the techniques described in this study are based on chirped pulses. Therefore, the nature of chirping of ultrafast laser pulses is first discussed and then chirped-pulse single-shot measurement methods and the photonic time-stretch method are explained. Furthermore, pulse propagation in an optical fiber is explained and our experimental setup for high-repetition-rate single-shot spectroscopy is introduced.

2.1 Chirped Pulse and Group Delay Dispersion

The nature of the chirpa chirped pulse is explained based on the description in *Femtosecond Laser Pulse: Principles and Experiments* by C. Rullière (Springer, 2005) [1]. First, to simplify the calculation, we assume a Gaussian function as the electric field of the pulse waveform from the pulse laser, E_y, as follows:

$$E_y(t) = \mathrm{Re}\left[E_0 e^{-\Gamma t^2 + \mathrm{i}\omega_0 t}\right], \tag{2.1.1}$$

where Γ is the shape factor of the Gaussian envelope, and ω_0 is the central angular frequency of the Gaussian pulse. If the phase of the pulse obeys a quadratic law in time:

$$E_y(t) = \mathrm{Re}\left[E_0 e^{-\Gamma t^2 + \mathrm{i}\left(\omega_0 t - \alpha t^2\right)}\right]. \tag{2.1.2}$$

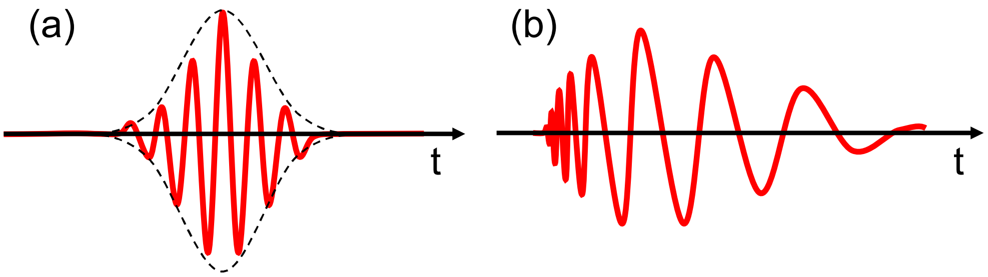

Figure 2.1 | (a) Time evolution of the electric field in a Gaussian pulse. (b) Time evolution of the electric field after chirping.

If the instantaneous angular frequency varies linearly with time:

$$\omega(t) = \frac{\partial \Phi}{\partial t} = \omega_o + \alpha t, \quad \alpha > 0. \tag{2.1.3}$$

These relationships indicate that the instantaneous frequency is redder in the leading part of the pulse and bluer in the trailing part, as shown in Figure 2.1. Such a changing optical frequency is called a “chirp.”

In addition to the chirp described above, the optical pulse shot propagating through a transparent medium simultaneously causes waveform distortion due to group velocity dispersion (GVD). We continue to consider the case of Gaussian pulse propagation in a transparent medium. The Fourier transform frequency of a Gaussian pulse in Eq. (2.1.1) is described below:

$$E_0(\omega) = e^{\frac{-(\omega-\omega_0)^2}{4\Gamma}} . \tag{2.1.4}$$

After the pulse propagates a distance x, and when we assume that $\Delta\omega \ll \omega_0$, the pulse spectrum becomes:

$$E(\omega, x) = e^{\left\{-\mathrm{i}k(\omega_0)x - \mathrm{i}k' x(\omega-\omega_0) - \left(\frac{1}{4\Gamma} + \frac{\mathrm{i}}{2}k''\right)(\omega-\omega_0)^2\right\}}, \tag{2.1.5}$$

where $k(\omega)$ is a frequency-dependent propagation factor. Using the inverse Fourier transform, we can get the time evolution of the electric field:

$$\varepsilon(t, x) = \sqrt{\frac{\Gamma(x)}{\pi}} e^{\left\{\mathrm{i}\omega_0\left(t - \frac{x}{v_\phi(\omega_0)}\right)\right\}} \times e^{\left\{-\Gamma(x)\left(t - \frac{x}{v_g(\omega_0)}\right)^2\right\}}, \tag{2.1.6}$$

where

$$v_\phi(\omega_0) = \left(\frac{\omega}{k}\right)_{\omega_0}, v_g(\omega_0) = \left(\frac{\mathrm{d}\omega}{\mathrm{d}k}\right)_{\omega_0}, \frac{1}{\Gamma(x)} = \frac{1}{\Gamma} + 2\mathrm{i}k''x. \tag{2.1.7}$$

In the first and second terms of Eq. (2.1.6), v_ϕ and v_g represent the phase velocity and the group velocity of the Gaussian pulse, respectively. When we introduce the propagation factor, $k = 2\pi/\lambda$, and the wavelength in the medium, $\lambda = 2\pi c/\omega n(\omega)$, into Eq. (2.1.7), we get

$$v_g \approx v_\phi \left(1 - \frac{\omega}{n(\omega)} \frac{\mathrm{d}n(\omega)}{\mathrm{d}\omega}\right). \tag{2.1.8}$$

The second term in Eq. (2.1.6) also shows that the pulse envelope is distorted during its propagation because its form factor, $\Gamma(x)$, depends on the angular frequency ω through k'':

$$k'' = \left(\frac{\mathrm{d}^2 k}{\mathrm{d}\omega^2}\right)_{\omega_0} = \frac{\mathrm{d}}{\mathrm{d}\omega}\left(\frac{1}{v_g}\right)_{\omega_0}. \tag{2.1.9}$$

This term is called GVD. In summary, the propagation of short optical pulses through a transparent medium result in pulse delays, duration spreads, and frequency chirp.

2.2 Chirped-Pulse Single-Shot Method

In this section, we introduce the concept of the chirped-pulse singe-shot method. Figure 2.3 shows the experimental setup for a single-shot method using a chirped pulse [2-4]. In this technique, the probe pulse from a laser source is chirped by transmitting it through a dispersive medium or using a diffraction grating pair to impart a chirp; each frequency of the probe pulse gives a different time delay. Then, the chirped pulse is irradiated on to the sample and the response of the sample is recorded in the spectral region of the probe pulse. Particularly, the time response at the sample is translated into the wavelength of the probe pulse. Finally, the modulated chirp pulse is entered into the spectrometer, and the response waveform is detected by measuring the spectral shape of the probe pulse.

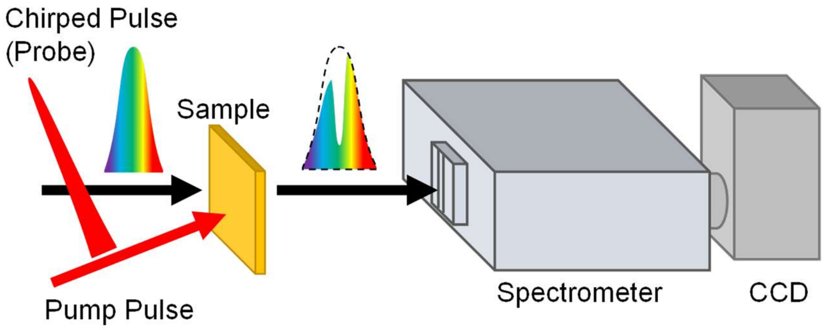

Figure 2.3 | Typical experimental setup for the single-shot method using chirped pulse.

The theoretical understanding of this method is described below. When we assume that the electric field of the probe pulse is expressed as $E_{pr}(t)$ and the probe pulse is modulated by the electric field of the pump pulse, $E_{pm}(t)$, the modulated pulse electric field, $E_m(t)$, is expressed as follows [2,3]:

$$\begin{aligned} E_m(t) &= \left[1 + \alpha E_{pm}(t)\right] E_{pr}(t) \\ &= E_{pr}(t) + \alpha E_{pm}(t) E_{pr}(t)\,, \end{aligned} \tag{2.2.1}$$

where α is the coefficient representing conversion processes. Therefore, the intensity of the modulated spectrum at the spectrometer, $I_m(\omega)$, is represented as

$$\begin{aligned} I_m(\omega) &= \left|\tilde{E}_m(\omega)\right|^2 \\ &= \left|\tilde{E}_{pr}(\omega)\right|^2 + \left|\tilde{E}_{sig}(\omega)\right|^2 \\ &\quad + \tilde{E}^*_{pr}(\omega)\tilde{E}_{sig}(\omega) + \tilde{E}_{pr}(\omega)\tilde{E}^*_{sig}(\omega), \end{aligned} \tag{2.2.2}$$

where

$$\tilde{E}_{pr}(\omega) = \int E_{pr}(t) e^{\mathrm{i}\omega t}\,\mathrm{d}t, \tag{2.2.3}$$

$$\tilde{E}_{sig}(\omega) = \int E_{pm}(t) E_{pr}(t) e^{\mathrm{i}\omega t}\,\mathrm{d}t \tag{2.2.4}$$

are the Fourier transforms of $E_{pr}(t)$ and $E_{sig}(t) = E_{pm}(t)E_{pr}(t)$, respectively. In this spectral encoding method, we reconstruct the pump signal as

$$E_{pm}(t) = \frac{\Delta I[\omega(t)]}{I_{pr}[\omega(t)]} = \frac{I_{sig}[\omega(t)] - I_{pr}[\omega(t)]}{I_{pr}[\omega(t)]}, \tag{2.2.5}$$

where $I_{sig}[\omega(t)] = \left|\tilde{E}_{sig}(\omega)\right|^2$, $I_{pr}[\omega(t)] = \left|\tilde{E}_{pr}(\omega)\right|^2$, and $\omega(t) = \omega_0 + bt$ is the probe instantaneous frequency. Here, ω_0 is the central angular frequency, and b is the chirp coefficient.

According to Refs. [2] and [4], the time resolution in this method is limited by the spectral width of the probe light and can be approximated by the square root of the product of the pre-chirp and post-chirp pulse widths. In their reports, the time resolution, τ_{res}, is expressed as follows:

$$\tau_{res} \sim \delta t \sim \sqrt{\tau_0 \tau_c}, \tag{2.2.6}$$

where δt is the applied pulse window, and τ_0 and τ_c are the transform-limited (un-chirped) and chirped pulse widths, respectively.

One of the features of the chirped pulse single-shot method is that the time window of the probe pulse is determined by the pulse width and the amount of chirp, as described above. Therefore, compared to other single-shot methods such as real-time pump-probe imaging spectroscopy [5] and echelon methods [6,7], we can easily change the time window according to the measurement object. Additionally, since the probe pulse can be focused to the diffraction limit on the sample, we can measure ultrafast phenomena on the sample by examining its microstructure, as discussed in Chapter 5.

2.3 Theory of the Photonic Time-Stretch Method

In this section, we introduce the theory of the photonic time-stretch method based on the description provided in *Photonic Time Stretch and Its Application to Analog-to-Digital Conversion* by F. Coppinger, A. S. Bhushan, and B. Jalali (IEEE Transactions on microwave theory and techniques **47,** 7 (1999)) [8].

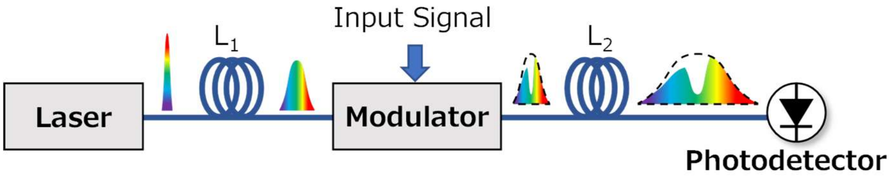

Figure 2.4 | Schematic description of the photonic time-stretch system [8].

Using the experimental setup shown in Figure 2.4, we consider the time stretch system when an ultrashort Gaussian pulse is modulated by an electrical input signal. After propagation through the first optical fiber of length L_1, the electric field can be represented by

$$E_{ch}(L_1, t) = e^{-\frac{t^2}{\tau^2}} \times e^{-\frac{\mathrm{i}t^2}{2L_1\beta_2}}, \tag{2.3.1}$$

and the electric field in the frequency domain is:

$$E_{ch}(L_1, f) = \frac{\sqrt{\pi}}{\left|\sqrt{\tau^{-2} + \frac{\mathrm{i}}{2L_1\beta_2}}\right|} e^{\left(\frac{-\pi^2 f^2}{\tau^{-2} + \frac{\mathrm{i}}{2L_1\beta_2}}\right)} \tag{2.3.2}$$

where β_2 is the second derivative of the propagation constant and 2τ is the $1/e$ width of the Gaussian pulse after dispersion [9]. When we consider that the chirp pulse is modulated with a sinusoid (the frequency and modulation depth are f_m and a, respectively) [8], the modulated field is given by

$$E_{in}(L_1, t) = E_{ch}(L_1, t) \times [1 + a\cos(2\pi f_m t)], \tag{2.3.3}$$

where we neglect the harmonics of f_m. When the modulated electric field passes through the second optical fiber with a length of L_2, the output electric field is represented as

$$E_{out}(L_1 + L_2, f) = E_{ch}(L_1, f) \times e^{\mathrm{i}2\pi^2 L_2 \beta_2 f^2} \tag{2.3.4}$$

and the electric field in time domain is given by

$$\begin{aligned} E_{out}(L_1 + L_2, t) &= \sqrt{M^{-1}} \times e^{\frac{-t^2}{(\tau M)^2}} \times e^{\frac{-\mathrm{i}t^2}{2(L_1+L_2)\beta_2}} \\ &\times \left[1 + \frac{a}{2}\left\{e^{\mathrm{i}\frac{Ft}{M}} + e^{-\mathrm{i}\frac{Ft}{M}}\right\} \times e^{\mathrm{i}\frac{\pi L_2 \beta_2 f_m F}{M}}\right], \end{aligned} \tag{2.3.5}$$

where $M = (L_1 + L_2)/L_1$ is the stretch factor, and $F = 2\pi f_m$. Therefore, the light intensity detected by the photodetector is calculated by the square absolute of Eq. (2.3.5), as follows:

$$\begin{aligned} I_{out}(L_1 + L_2, t) &\propto E_{out}(L_1 + L_2, t) \times E^*_{out}(L_1 + L_2, t) \\ &= \frac{1}{M} e^{\frac{-2t^2}{(\tau M)^2}} \times \left[1 + 2a \cdot \cos\left(\frac{Ft}{M}\right) \cdot \cos\left(\frac{\pi L_2 \beta_2 f_m F}{M}\right)\right]. \end{aligned} \tag{2.3.6}$$

Equation (2.3.6) represents the transformation undertaken by an electrical signal during the photonic time-stretch process with an optical fiber. From Ref. [8], the first cosine function $\cos(Ft/M)$ in Eq. (2.3.6) shows that the frequency is reduced by the stretch factor M, which depends on the ratio of the total dispersion of the experimental setup. This indicates that the high-frequency signal can be down-converted and detected with a photodetector using the photonic time-stretch method.

2.4 Experimental Setup Concepts

In this section, we introduce the conceptual background of the experiment setup. Figure 2.5 shows a schematic of our high-repetition-rate single-shot detection method. We have developed this new single-shot method by combining a chirped-pulse single-shot method [2-4] with a photonic time-stretch method [8,10-12]. An explanation of the underlying principles as follows.

First, the time response of the sample induced by the pump pulse is encoded to the spectrum of the chirped probe pulse. In Figure 2.5, since we assume a pump-probe measurement using a high-repetition-rate single-shot method, the transient transmittance change induced by the pump pulse is encoded as a time response of the sample. Second, the modulated probe pulse enters an optical fiber and is further chirped to extend the waveform timescale from several picoseconds to a nanosecond. Finally, the extended waveform is converted into an electrical signal, using a high-speed photodiode, and the waveform is observed on a digital real-time oscilloscope. The waveform is normalized by the reference probe pulse, and a

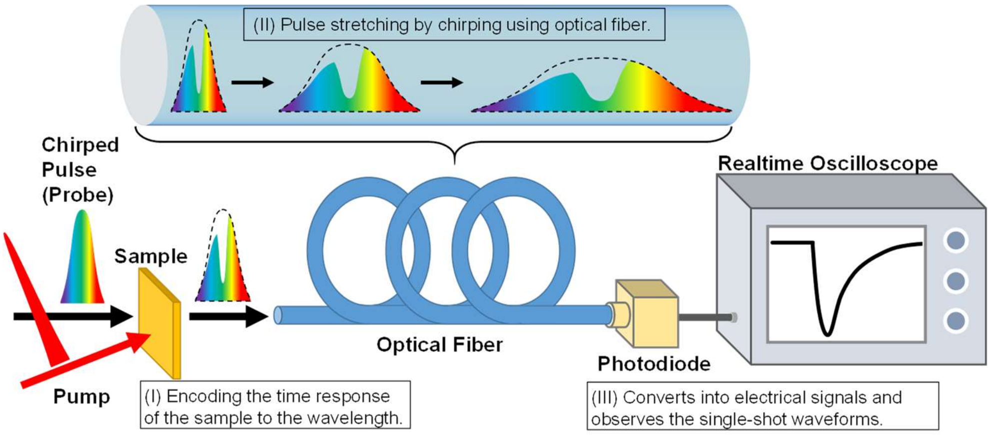

Figure 2.5 | Schematic illustrating the basic concepts of our high repetition-rate single-shot detection scheme.

single-shot response waveform is obtained. Because the frame rate, with the combination of a photodiode and oscilloscope, is much higher than that of a CCD or CMOS camera used in a conventional single-shot measurement method [2-7], we can obtain tens of thousands of single-shot measurements per second, depending on the repetition of the laser source.

Our single-shot method enables the simultaneous measurement of two different timescales. This is because femtosecond-to-picosecond time information is continuously acquired per pulse, depending on the repetition rate of the laser, as shown in Figure 2.6. This allows us to track and visualize the changes in the ultrafast response of a sample over a wide time range. For example, long-lifetime relaxation with strong single-pulse excitation, with high temporal resolution, and the accumulation effect with multi-pulse irradiation can be observed. Therefore, this method reveals the relationship between the ultrafast response due to photoexcitation and long-term responses associated with structural changes. It also provides new insights into photoinduced phase change and optical processing.

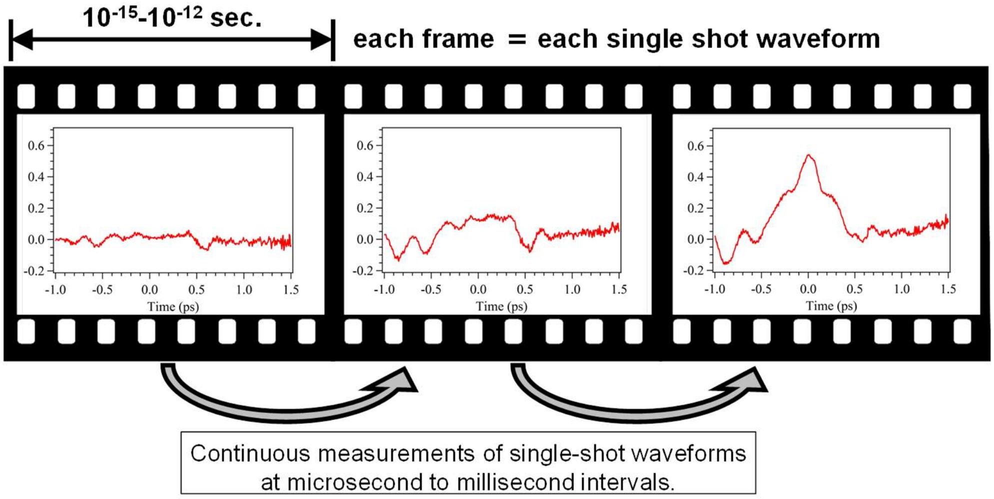

Figure 2.6 | Our single-shot method continuously acquires femtosecond to several picosecond time information per pulse depending on the repetition rate of the laser.

References

[1] C. Rullière, “Femtosecond laser pulses principles and experiments second edition,” Springer (2005).

[2] K. Y. Kim, B. Yellampalle, G. Rodriguez, R. D. Averitt, A. J. Taylor, and J. H. Glownia, “Single-shot, interferometric, high-resolution, terahertz field diagnostic,” App. Phys. Lett. **88**, 041123 (2006).

[3] B. Yellampalle, K. Y. Kim, G. Rodriguez, J. H. Glownia, and A. J. Taylor, “Algorithm for high-resolution single-shot THz measurement using in-line spectral interferometry with chirped pulses,” App. Phys. Lett. **87**, 211109 (2005).

[4] J.-P. Geindre, P. Audebert, S. Rebibo, and J.-C. Gauthier, “Single-shot spectral interferometry with chirped pulses,” Opt. Lett. 26, 1612 (2001).

[5] N. Furukawa, C. E. Mair, V. D. Kleiman, and J. Takeda, “Femtosecond real-time pump-probe imaging spectroscopy,” App. Phys. Lett. **85,** 4645 (2004).

[6] G. P. Wakeham, and K. A. Nelson, “Dual-echelon single-shot femtosecond spectroscopy.” Opt. Lett. **25**, 505 (2000).

[7] Y. Minami, Y. Hayashi, J. Takeda, and I. Katayama, “Single-shot measurement of a terahertz electric-field waveform using a reflective echelon mirror,” Appl. Phys. Lett. **103,** 051103 (2013).

[8] F. Coppinger, A. S. Bhushan, and B. Jalali, “Photonic time stretch and its application to analog-to-digital conversion,” IEEE Transactions on microwave theory and techniques **47,** 7 (1999).

[9] G. P. Agrawal, “Nonlinear fiber optics fifth edition,” Academic Press (2012).

[10] K. Goda, K. K. Tsia and B. Jalali, “Serial time-encoded amplified imaging for real-time observation of fast dynamic phenomena,” Nature 458, 7242, 1145 (2009).

[11] K. Goda, B. Jalali, “Dispersive Fourier transformation for fast continuous single-shot measurements,” Nat. Photonics 7, 102 (2012).

[12] C. Lei, B. Guo, Z. Cheng, and K. Goda, “Optical time-stretch imaging: Principles and applications,” Appl. Phys. Rev. **3,** 011102 (2016).

Chapter 3

Demonstration of High-Repetition Rate Single-Shot Method

3.1 Introduction

In this chapter, we demonstrate our high-repetition single-shot method using a long optical fiber, a photodiode, and an oscilloscope [1]. The GVD of the fiber elongates the picosecond pulse to the nanosecond range [2,3], enabling us to observe picosecond dynamics as an analog of high-frequency signals, which can be detected using an oscilloscope. Using this method, we report an example of this new technique by recording the power dependence of an ultrafast optical Kerr measurement in lithium niobate ($LiNbO_3$) in one second.

3.2 Experimental Methods

3.2.1 Optical Kerr Effect

By combining an optical Kerr medium with a polarizer, as shown in Figure 3.1, we can make a device where the probe light is transmitted only when the excitation light is incident [4,5]. We call such a device optical Kerr shutter or optical Kerr gate.

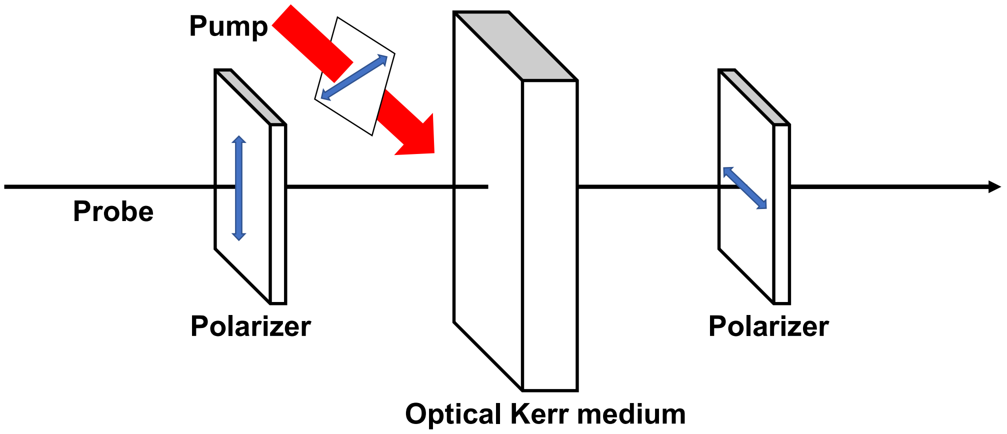

Figure 3.1 | Layout of optical Kerr shutters [5].

By using ultrashort laser pulses for excitation, we can create an ultrafast optical shutter that opens less than a few picoseconds, and it is used for the observation of ultrafast phenomena. In addition, since the polarized light is generally very sensitive, optical Kerr shutters are also used to evaluate the magnitude of the optical Kerr effect of nonlinear optical media and their time response [5].

We consider the case of the optical Kerr effect when a probe beam is entered into an optical Kerr medium sandwiched between two polarizers, one transmitting only y-axis polarization and the other x-axis polarization. The electric field of the incident probe light is defined as follows:

$$\boldsymbol{E}^{\mathrm{pr}}(\boldsymbol{r},t)=\frac{1}{2}E_0^{\mathrm{pr}}e^{\mathrm{i}(\boldsymbol{k}\cdot\boldsymbol{r}-\omega t)}+c.c, \tag{3.2.1}$$

$$E_0^{\mathrm{pr}}=\begin{pmatrix}E_x^{(\omega)}\\ E_y^{(\omega)}\end{pmatrix}=\begin{pmatrix}0\\ E_0^{\mathrm{pr}}\end{pmatrix}. \tag{3.2.2}$$

If we assume the excitation light $\boldsymbol{E}^{\mathrm{p}}(\boldsymbol{r},t)$ is linearly polarized in the direction of $\pi/4$ with respect to the x-axis and we define the nonlinear polarization $\boldsymbol{P}^{(3)}(\boldsymbol{r},t)$ with angular frequency ω and wavenumber vector $\boldsymbol{k}$, the generated electric field is

$$E_x^{(3)}(\boldsymbol{r},t)=\frac{1}{2}E_{\mathrm{sig}}e^{\mathrm{i}(\boldsymbol{k}\cdot\boldsymbol{r}-\omega t)}+c.c \tag{3.2.3}$$

$$E_{\mathrm{sig}}=\frac{\mathrm{i}Z_0\omega}{2n(\omega)}P_x^{(\omega)}L=\frac{3\mathrm{i}\omega L}{8cn(\omega)}\left(\chi_{xxxx}^{(3)}-\chi_{xxyy}^{(3)}\right)E_0^{\mathrm{pr}}\left|E_0^{\mathrm{p}}\right|^2 \tag{3.2.4}$$

where L is the length of the optical Kerr medium, $n(\omega)$ is the linear refractive index, Z_0 is the impedance of the vacuum, $\chi^{(3)}_{xxxx}$ and $\chi^{(3)}_{xxyy}$ are the third-order nonlinear susceptibility, while the absorption and reflection at the end surface are ignored. Since the light intensity, I_{sig}, detected as a signal is proportional to $\left|E_{\mathrm{sig}}\right|^2$, using Eq. (3.2.4), I_{sig} is expressed as follows:

$$I_{\mathrm{sig}} = \frac{n}{2Z_0}\left|E_{sig}\right|^2 \propto \left|\chi^{(3)}_{xxxx} - \chi^{(3)}_{xxyy}\right|^2 (I^{\mathrm{p}})^2 I^{\mathrm{pr}} \qquad (3.2.5)$$

This indicates that I_{sig} is proportional to the square of the absolute value of the nonlinear susceptibility, E_{sig}, the square of the excitation intensity, I^{p}, and the probe light intensity, I^{pr}. When an imaginary part of the nonlinear susceptibility is present, the absorption coefficients caused by the nonlinear optical effects have anisotropy, which also contributes to the signal strength.

3.2.2 Characteristics of $LiNbO_3$ Crystal

In this chapter, we investigate the pump power dependence of the optical Kerr effect in the $LiNbO_3$ crystal using high-repetition-rate single-shot spectroscopy. Here, we introduce the characteristic features of the $LiNbO_3$ crystal.

$LiNbO_3$ is a ferroelectric crystal used in numerous photonic devices [6,7]. The loss of inversion symmetry allows and enhances the optical nonlinearities, such as sum and difference frequency generation, the optical Kerr effect, and excitation of polaritons with ultrafast near-infrared (NIR) laser pulses [8-11]. These nonlinearities are important to design future optoelectronic devices.

The $LiNbO_3$ crystal is a ferroelectric ternary crystal of a 3m point group and shows ferroelectricity at room temperature [12]. Its melting point is $T_m = 1247$ ℃, and it transforms from the ferroelectric phase to the dielectric phase at (Curie temperature) $T_c \sim 1210$ ℃ [12]. The crystal structure of the $LiNbO_3$ crystal in the ferroelectric phase involves three O-atom planes, one Li ion, and one Nb ion (Figure 3.2). The Nb ion is slightly shifted from the center of the two O-atom arrangement planes. Therefore, $LiNbO_3$ has lost its inversion symmetry and has spontaneous polarization in the c-axis direction of the crystal. Its refractive index is a negative uniaxial crystal $(n_o > n_e)$ and is expressed using the Sellmeier dispersion formula as follows [13]:

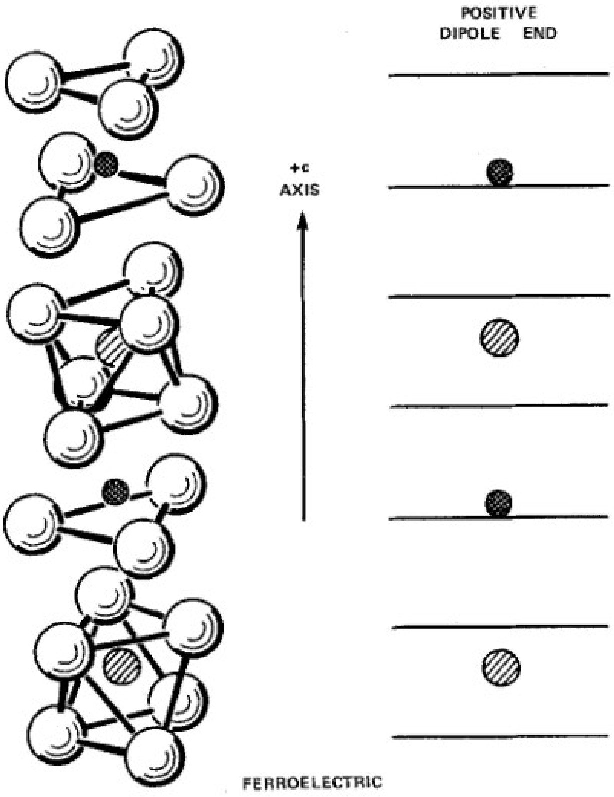

Figure 3.2 | Positions of the lithium atoms and niobium atoms with respect to the oxygen octahedra in ferroelectric lithium niobate [12]. Adapted from Ref. [12].

$$n_e^2 - 1 = \frac{2.9804\lambda^2}{\lambda^2 - 0.02047^2} + \frac{0.5981\lambda^2}{\lambda^2 - 0.0666^2} + \frac{8.9543\lambda^2}{\lambda^2 - 416.08^2} \tag{3.2.6}$$

$$n_o^2 - 1 = \frac{2.6734\lambda^2}{\lambda^2 - 0.01764^2} + \frac{1.2290\lambda^2}{\lambda^2 - 0.05914^2} + \frac{12.614\lambda^2}{\lambda^2 - 474.6^2} \tag{3.2.7}$$

where λ is the wavelength in μm scale.

3.2.3 Experimental Setup

Figure 3.3 shows the experimental setup used in this chapter. We used a Ti:Sapphire regenerative amplifier with 40-fs pulse duration, 1-kHz repetition rate, 1.4-mJ output power, and 800-nm center wavelength. The laser was divided into pump and probe beams by using a beam splitter. The intensity of the pump pulse was rapidly scanned by computer-controlled rotation of a half-wave plate placed

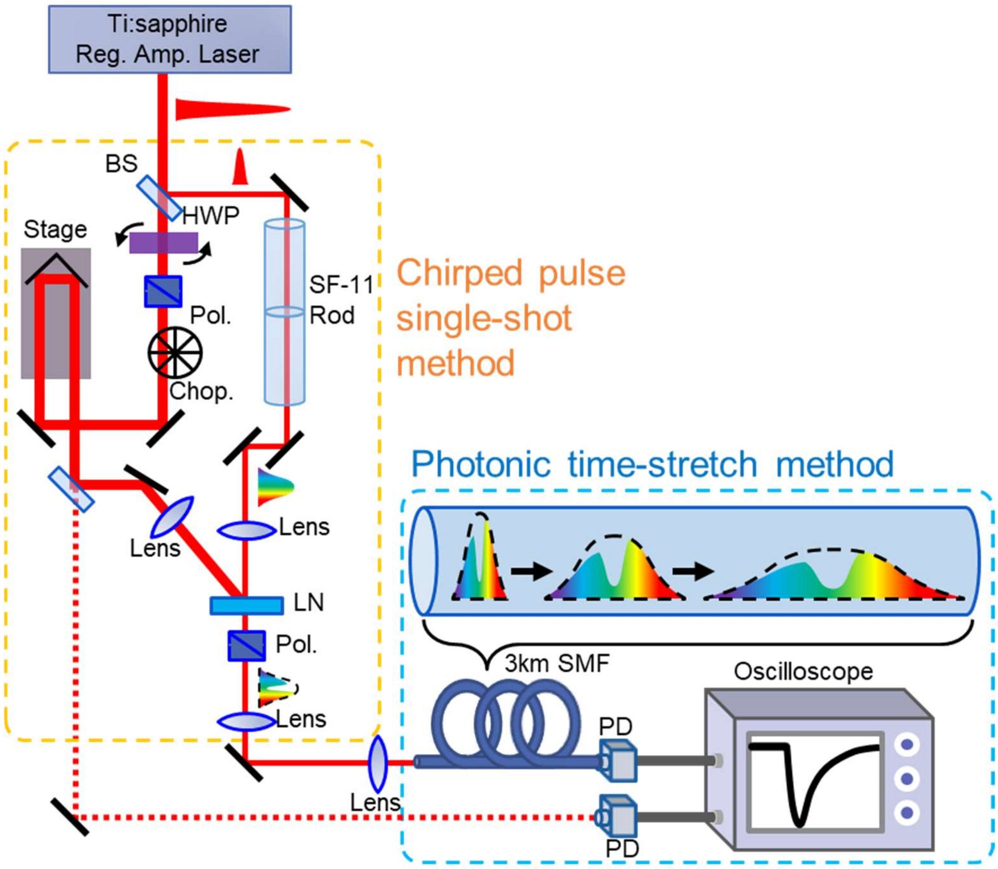

Figure 3.3 | Experiment setup for measuring the power dependence of the ultrafast optical Kerr effect in $LiNbO_3$. BS: beam splitter, HWP: half-wave plate, Pol.: polarizer, Chop.: optical chopper, LN: $LiNbO_3$ crystal, SMF: single-mode fiber, PD: photodiode.

before a polarizer. In addition, the pump pulse was chopped at 500 Hz by an optical chopper. The intensity of the pump pulse was detected by a fast photodiode (ThorLabs DET02AFC, Si, wavelength: 400-1100 nm, 3-dB bandwidth: 1.2 GHz) and monitored by a real-time oscilloscope (Tektronix DPO71244C, bandwidth: 12.5 GHz, sample rate: 50–100 GS/s).

On the other hand, the probe pulse was passed through a 150-mm SF-11 glass rod twice to induce positive chirp with ~4-ps pulse duration. The pump and probe pulses were then focused on a 1-mm-thick X-cut $LiNbO_3$ single crystal with polarizations oriented 45 degrees with respect to each other. To make the optical Kerr shutter system, a polarizer was placed behind the $LiNbO_3$ crystal. When the $LiNbO_3$ crystal was lamped by the pump pulse, the polarization of the probe pulse was rotated to modulate the intensity. Therefore, the time response of the optical

Kerr effect induced by the pump pulse was encoded into the wavelength of the chirped probe pulse, as shown in Figure 3.3, based on the chirped pulse single-shot technique [14,15].

Then, the modulated probe pulses were input into a 3-km-long single-mode fiber (Nufern, 780-OCT) to further extend into nanosecond timescale. Then, the intensity profile of the probe pulse was recorded using a photodiode and a real-time oscilloscope based on the photonic time-stretch method [2,3].

The main features of this optical system include the combination of the chirped-pulse single-shot method and the photonic time-stretch method using long fibers. Further, we can simultaneously monitor the waveform change of the probe pulse and the intensity change of the pump pulse. Thus, by simultaneously acquiring the pump and probe pulse, we can continuously acquire the dynamics for each excitation density.

3.3 Results and Discussion

Figure 3.4 shows the typical intensity profile of the probe pulses. The red line shows the reference probe pulse without a pump pulse, and the blue line shows the modulated probe pulse with the optical Kerr effect. The difference between these waveforms indicates the observation of an optical Kerr signal. The probe pulse duration was further expanded from ~4 ps to ~20 ns due to the GVD in the 3-km-long single-mode fiber.

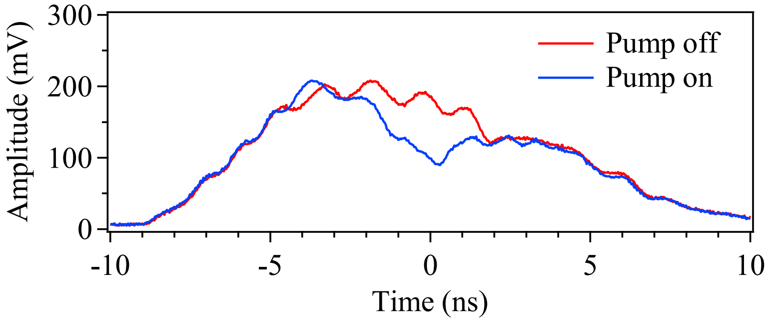

Figure 3.4 | The typical intensity profile of the probe pulses with (red) and without (blue) a pump pulse observed directly at the photodiode. The difference between these waveforms indicates the observation of an optical Kerr signal.

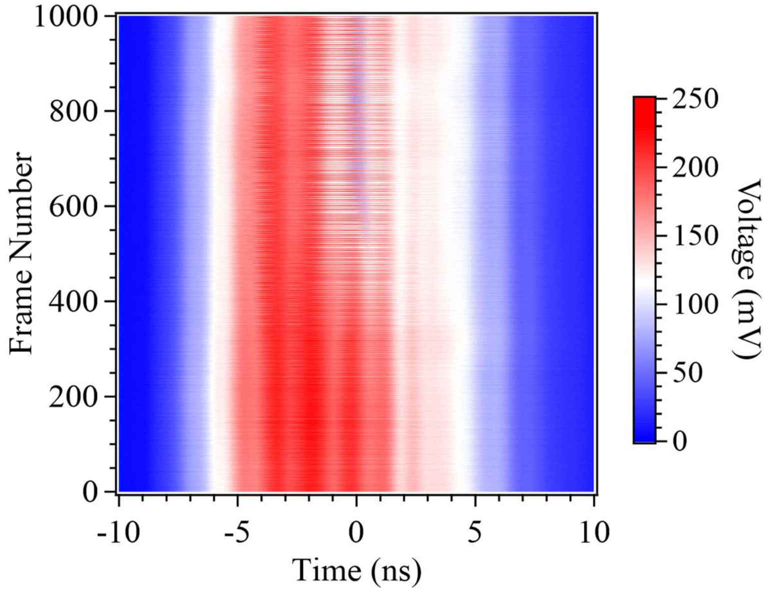

Figure 3.5 | 2D image of 1000 single-shot waveforms per second. The horizontal axis, the vertical axis, and the color shading corresponds to the time axis of probe pulse profiles, the number of each frame, and the amplitude of the waveforms, respectively.

To minimize the pulse-to-pulse fluctuation of the laser intensity, we chopped the pump pulses at 500 Hz. Therefore, we obtained 500 waveforms as the reference (without pump) and the other 500 waveforms as the signal (with pump) within 1 second. Figure 3.5 shows a 2D map obtained by aligning a total of 1000 waveforms. The horizontal axis of the map corresponds to the time axis of probe pulse profiles, and the vertical axis shows the number of each frame repeated at 1 kHz. The color scale corresponds to the amplitude of the waveforms.

Then, to examine the optical Kerr signal, $\Delta I(t)/I(t)$, we normalized each signal probe waveform (coincident with the pump) using the reference probe profiles as follows:

$$\frac{\Delta I(t)}{I(t)} = \frac{I_{sig}(t) - I_{ref}(t)}{I_{ref}(t)}, \tag{3.3.1}$$

$$I_{ref}(t) = \frac{I_{r\_before} + I_{r\_after}}{2} \tag{3.3.2}$$

where $I_{sig}(t)$ is the signal probe waveform coincident with the pump pulse, and $I_{ref}(t)$ is the average of two probe profiles without the pump, where I_{r_before} is the reference probe immediately before the pump pulse and I_{r_after} is the one after

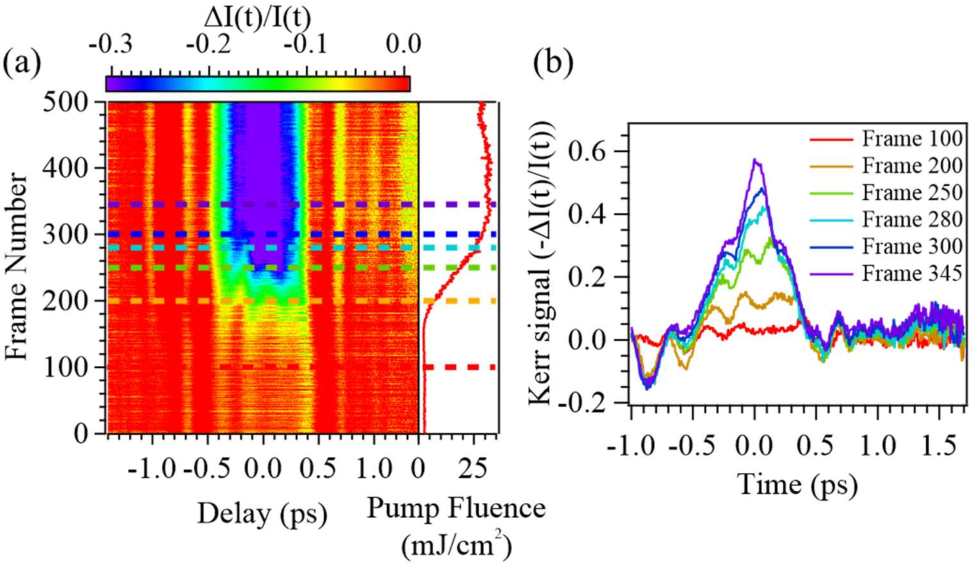

Figure 3.6 | (a) 500 normalized optical Kerr signal traces (ΔI/I) of $LiNbO_3$ (left) captured while changing the pump intensity (right). The time axis of the traces is calibrated by measuring two waveforms while changing the pump delay time. (b) Slices of the optical Kerr waveforms from the dashed lines in (a).

the pump pulse. Figure 3.6(a) shows the 2D map obtained by aligning 500 normalized optical Kerr signal traces (left side). The time axis of the traces was calibrated to picosecond timescale by changing the pump delay time and measuring two waveforms. The right side of Figure 3.6(a) shows the pump intensity as a function of the frame number, which is monitored with PD taken by the same oscilloscope. The pump intensity was ramped up during the measurement from 2.3 mJ/cm^2 to 31 mJ/cm^2. As shown in Figure 3.6(a) and 3.6(b), we see a clear change in the optical Kerr signal intensity as the number of frames or the pump intensity increases. Additionally, some fringes were observed around the Kerr signal in these waveforms such as -0.85 or 0.7 picoseconds in Figure 3.6. These may be due to the waveform distortions in the time-encoding technique [16].

To examine the correlation between the intensity of the optical Kerr effect and the pump intensity, we plotted the peak intensity of the optical Kerr signal at the time origin as a function of pump intensity, as shown in Figure 3.7. The optical Kerr signal grows quadratically, in line with the $\chi^{(3)}$ nonlinearity of the material. Based

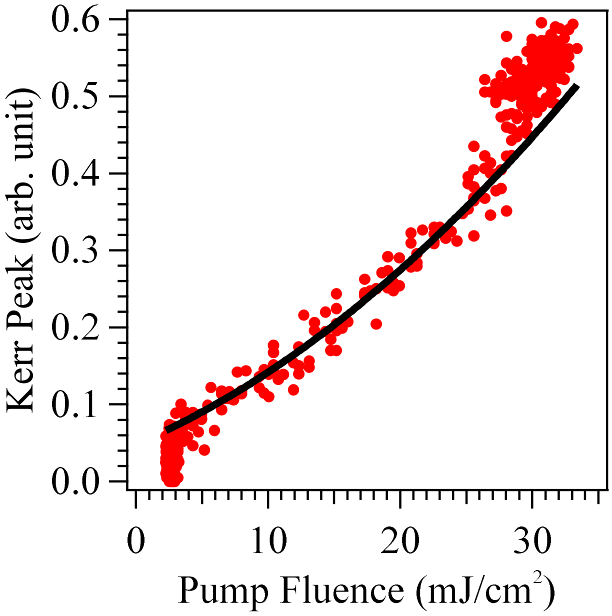

Figure 3.7 | Power dependence of the peak intensity of the optical Kerr signal at the time origin extracted from the data shown in Figure 3.6. The black solid line indicates the quadratic fitting expected for the optical Kerr nonlinearity.

on Eq. (3.2.5), when the probe pulse intensity was almost constant, the relationship between the intensity of the optical Kerr signal and pump intensity is rewritten as

$$I_{Kerr} \propto \mathrm{X}^{(3)^2} |I^{\mathrm{p}}|^2, \qquad \mathrm{X}^{(3)} = \chi^{(3)}_{xxxx} - \chi^{(3)}_{xxyy}\,. \tag{3.3.3}$$

The black solid line in Figure 3.7 indicates the quadratic fitting expected for the optical Kerr nonlinearity, and we estimate the magnitude of the nonlinear refractive index to be 4.2×10^{-13} esu, which agrees well with the previous reports on $\mathrm{LiNbO_3}$ [17].

Finally, we note the pulse duration of the optical Kerr signal. As shown in Figure 3.6(b), the pulse duration of the optical Kerr signal was longer than that of the pump pulse. One possible reason is the signal distortions in the chirped pulse detection method [18], which is caused by the interference between the sum or differential frequency signal of the pump pulse and the probe pulse. Additionally, the other possible cause of the problem is the limited time resolution of the probe pulse and the bandwidth of the photodiode. In this experiment, the temporal resolution of the chirped probe pulse was estimated as ~400 fs from Eq. (2.2.6), and the bandwidth was limited to 1 GHz due to the photodiode.

3.5 Conclusion in Chapter 3

We demonstrated the high-repetition-rate single-shot measurements of ultrafast optical Kerr signals in $LiNbO_3$ crystal using a long optical fiber, a single photodiode, and an oscilloscope. Since the signal modulation was mapped onto the wavelength of the chirped pulses, it can be expanded to timescales easily measured with a fast oscilloscope. Additionally, we obtained the full information on the intensity dependence of the optical Kerr signals within one second using the oscilloscope. Using conventional time-domain or single-shot spectroscopy would have required repeating the measurements and taking at least a few minutes to obtain a large number of waveforms to get the same results on the intensity dependence of the optical Kerr signals. Therefore, these results may provide evidence for the superiority of our single-shot method over conventional approaches.

References

[1] M. Kobayashi, Y. Minami, C. L. Johnson, P. D. Salmans, N. R. Ellsworth, J. Takeda, J. A. Johnson and I. Katayama, "High-acquisition-rate single-shot pump-probe measurements using time-stretching method," Sci. Rep. 6, 37614 (2016).

[2] K. Goda, K. K. Tsia and B. Jalali, "Serial time-encoded amplified imaging for real-time observation of fast dynamic phenomena," Nature 458, 7242, 1145 (2009).

[3] K. Goda, B. Jalali, "Dispersive Fourier transformation for fast continuous single-shot measurements," Nat. Photonics 7, 102 (2012).

[4] R. W. Boyd, "Nonlinear optics, 3rd edition," Academic Press (2008).

[5] T. Hattori, "Introduction to nonlinear optics," SHOKABO Publishing, Tokyo (2009) (in Japanese).

[6] C. A. Werley, K. Fan, A. C. Strikwerda, S. M. Teo, X. Zhang, R. D. Averitt, and K. A. Nelson, "Time-resolved imaging of near-fields in THz antennas and direct quantitative measurement of field enhancements," Opt. Exp. 20, 8551 (2012).

[7] G. D. Miller, R. G. Batchko, W. M. Tulloch, D. R. Weise, M. M. Fejer, and R. L. Byer, "42%-efficient single-pass cw second-harmonic generation in periodically poled lithium niobate," Opt. Lett. 22, 1834 (1997).

[8] J. Hebling, G. Almási, I. Z. Kozma, and J. Kuhl, "Velocity matching by pulse front tilting for large-area THz-pulse generation," Opt. Exp. 10, 1161 (2002).

[9] H. Sakaibara, Y. Ikegaya, I. Katayama, and J. Takeda, "Single-shot time-frequency imaging spectroscopy using an echelon mirror," Opt. Lett. 37, 1118 (2012).

[10] Y. Ikegaya, H. Sakaibara, Y. Minami, I. Katayama, and J. Takeda, "Real-time observation of phonon-polariton dynamics in ferroelectric $LiNbO_3$ in time-frequency space," Appl. Phys. Lett. 107, 062901 (2015).

[11] T. Kuribayashi, T. Motoyama, Y. Arashida, I. Katayama, and J. Takeda, "Anharmonic phonon-polariton dynamics in ferroelectric $LiNbO_3$ studied with single-shot pump-probe imaging spectroscopy," J. Appl. Phys. 123, 174103 (2018).

[12] R. S. Weis and T. K. Gaylord, "Lithium niobate: Summary of physical properties and crystal structure," Appl. Phys. A 37, 191 (1985)

[13] D. E. Zelmon, D. L. Small, and D. Jundt, "Infrared corrected Sellmeier coefficients for congruently grown lithium niobate and 5 mol. % magnesium oxide–doped lithium niobate," J. Opt. Soc. Am. B. 14, 3319 (1997).

[14] K. Y. Kim, B. Yellampalle, G. Rodriguez, R. D. Averitt, A. J. Taylor, and J. H. Glownia, "Single-shot, interferometric, high-resolution, terahertz field diagnostic," App. Phys. Lett. 88, 041123 (2006).

[15] B. Yellampalle, K. Y. Kim, G. Rodriguez, J. H. Glownia, and A. J. Taylor, "Algorithm for high-resolution single-shot THz measurement using in-line spectral interferometry with chirped pulses," App. Phys. Lett. 87, 211109 (2005).

[16] I. A. Shkrob, D. A. Oulianov, R. A. Crowell, and S. Pommeret, "Frequency-domain "single-shot" ultrafast transient absorption spectroscopy using chirped laser pulses," J. Appl. Phys. **96,** 25 (2004).

[17] I. A. Kulagin, R. A. Ganeev, R. I. Tugushev, A. I. Ryasnyansky, and T. Usmanov, "Analysis of third-order nonlinear susceptibilities of quadratic nonlinear optical crystals," J. Opt. Soc. Am. B 23, 75 (2006).

[18] I. A. Shkrob, D. A. Oulianov, R. A. Crowell, and S. Pommeret, "Frequency-domain "single-shot" ultrafast transient absorption spectroscopy using chirped laser pulses," J. Appl. Phys. 96, 25 (2004).

Chapter 4

Improvement of Signal-to-Noise Ratio & Variable Time Window

4.1 Introduction

In the previous chapter, we demonstrated the high-repetition-rate single-shot measurement method using a long optical fiber, a fast photodiode, and a real-time oscilloscope. However, we also found some problems. First, we used a long optical fiber with a length of 3 km to temporally stretch the time-encoded spectrum of the probe pulse by the GVD, but the long fiber also degrades the signal-to-noise ratio because of the propagation losses of the probe pulses through it. This degradation has limited the performance of the applicable light source and observable phenomena. In addition, we used an SF-11 glass rod to pre-chirp the probe pulse, but this method normally fixes the amount of the chirp and makes it difficult to change the time window of the probe pulse.

To overcome these problems, we used a chirped fiber Bragg grating (CFBG) to temporally stretch the spectrum of the encoded probe pulses and a grating pair to facilitate changing the time window of the pump-probe traces [1]. By employing these changes, we examined the improvement in the noise level, the variability of the time window, and the temporal resolution of our single-shot method.

4.2 Experimental Methods

4.2.1 Chirped Fiber Bragg Grating (CFBG)

Fiber Bragg gratings (FBGs) are fibers that have longitudinal diffraction gratings in the core, which works as an optical filter due to Bragg reflection [2-4]. In CFBGs, differently from FBGs, the pitches of the diffraction grating are non-periodic as shown in Figure 4.1, and each diffraction grating reflects a specific wavelength and returns a broadband spectrum, depending on the grating length, to act like a chirped mirror [5]. CFBGs have been widely used as low-loss dispersive elements [6], optical communication systems [7], and sensor applications for mechanical engineering [8,9].

Generally, we can simulate and understand the propagation of the electric field in the CFBG using the transfer matrix method (TMM) [3]. This method is based on the coupled-mode theory (CMT), which is derived from Maxwell's equations. We explain the numerical treatment in CFBGs using the TMM based on Refs. [5] and [8]. We assume that the CFBG is divided into M sections, as shown in Figure 4.1. The amplitude of the output waveform is shown as follows:

$$\begin{bmatrix} A_M \\ B_M \end{bmatrix} = \boldsymbol{F} \begin{bmatrix} A_0 \\ B_0 \end{bmatrix}; \quad \boldsymbol{F} = \boldsymbol{F}_M \cdot \boldsymbol{F}_{M-1} \cdot \ldots \boldsymbol{F}_i \cdot \ldots \boldsymbol{F}_1 \tag{4.2.1}$$

where

$$\begin{bmatrix} A_i \\ B_i \end{bmatrix} = F_i \begin{bmatrix} A_{i-1} \\ B_{i-1} \end{bmatrix} = \begin{bmatrix} F_{11} & F_{12} \\ F_{21} & F_{22} \end{bmatrix} \begin{bmatrix} A_{i-1} \\ B_{i-1} \end{bmatrix}. \tag{4.2.2}$$

A_i and B_i are the amplitudes of the electric field after propagating through section i and the elements in each transfer matrix F_i have the following expression:

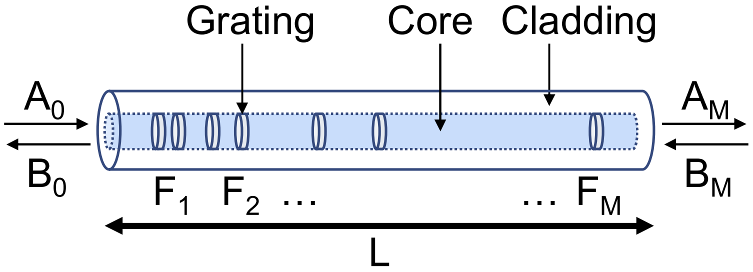

Figure 4.1 | Schematic of a CFBG structure [5].

$$F_i = \begin{bmatrix} \cosh(\gamma\Delta_z) - i\frac{\hat{\sigma}}{\gamma}\sin(\gamma\Delta_z) & -i\frac{\kappa}{\gamma}\sinh(\gamma\Delta_z) \\ i\frac{\kappa}{\gamma}\sinh(\gamma\Delta_z) & \cosh(\gamma\Delta_z) + i\frac{\hat{\sigma}}{\gamma}\sin(\gamma\Delta_z) \end{bmatrix}, \tag{4.2.3}$$

where Δ_z is the length of the ith section. The coefficient γ is defined as

$$\gamma = \sqrt{\kappa^2 - \hat{\sigma}^2} \tag{4.2.4}$$

where κ and $\hat{\sigma}$ are the local values in the ith section [8]. When a CFBG has a linear chirp profile, the chirp term can be explained as follows:

$$\frac{1}{2}\frac{\mathrm{d}\phi}{\mathrm{d}z} = -\frac{4\pi n_{eff} z}{\lambda_D^2}\frac{\mathrm{d}\lambda_D}{\mathrm{d}z} \tag{4.2.5}$$

where $\mathrm{d}\lambda_D/\mathrm{d}z$ is the changing rate of the wavelength with the position in the grating, usually given in units of nm/cm.

While the numerical analysis is carried out according to the above processes, in the actual production of CFBGs, non-periodic refractive index changes are formed by illuminating UV light through a phase mask to the optical fibers [10]. By designing the structure of the phase mask, we can determine the wavelength bandwidth of the CFBG. Depending on the direction of the incident light into the CFBG, it acts as a pulse compressor or a pulse stretcher and is used in the optical communications field as a compressor to compensate for pulsed light that has been stretched by dispersion. In this study, we used the CFBG as a pulse stretcher to reduce the propagation distance of the probe pulse in the fiber and investigate whether the CFBG is useful for improving the signal-to-noise ratio by suppressing the loss of signal intensity during the propagation.

4.2.2. Grating Pair

Grating pairs are usually used as a pulse compressor for chirped-pulse amplification (CPA) lasers [11-14]. We will explain how the grating pair works in this section based on Refs. [11] and [15]. To simplify the explanation, we use transmission gratings, G_1 and G_2, to compress or stretch a pulse waveform, as shown in Figure 4.2. The gratings G_1 and G_2 are set up parallel to each other, and we consider that the light with wavelength λ enters the grating G_1 at point A with an incidence angle γ, and the light is diffracted with an angle θ. Then, the

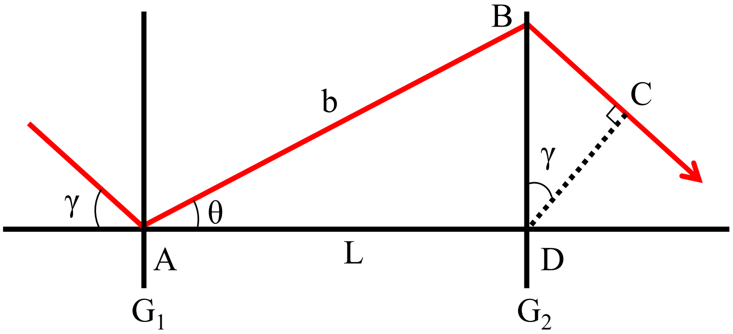

Figure 4.2 | Optical path through a pair of transmission gratings [11].

diffracted light is diffracted again by the grating G_2 at point B. In such a case, the diffraction due to a grating can be written as

$$d(\sin\gamma + \sin\theta) = \lambda. \tag{4.2.6}$$

To further simplify the wave propagation condition, we assume that the light only propagates in air. In this specific case, the group delay is equal to the travel time of light along ABC, therefore we can get the GVD and the dispersion parameter by applying a small-angle approximation as follows:

$$D = \frac{\lambda}{cd^2}\left[1 - \left(\frac{\lambda}{d} - \sin\gamma\right)^2\right]^{-1}, \tag{4.2.7}$$

$$k'' = -\frac{\lambda^3}{2\pi c^2 d^2}\left[1 - \left(\frac{\lambda}{d} - \sin\gamma\right)^2\right]^{-1}. \tag{4.2.8}$$

These parameters indicate that we can select a set them to design a pair of gratings producing a positive or a negative GVD. If we consider the second-order dispersion with material dispersion and the number of diffraction order m, the dispersion parameters are expressed as follows [15]:

$$k''_{str} = \frac{m^2\lambda^3 l_{str}}{4\pi c^2 d^2}\left[1 - \left(\frac{m\lambda}{d} - \sin\gamma_{str}\right)^2\right]^{-1}, \tag{4.2.9}$$

$$k''_{mat} = \frac{\lambda^3 l_{mat}}{2\pi c^2}\frac{\mathrm{d}^2 n}{\mathrm{d}\lambda^2}\bigg|_{\lambda}, \tag{4.2.10}$$

$$k''_{cmp} = \frac{-m^2\lambda^3 l_{cmp}}{4\pi c^2 d^2}\left[1 - \left(\frac{m\lambda}{d} - \sin\gamma_{cmp}\right)^2\right]^{-1}, \tag{4.2.11}$$

where k''_{str}, k''_{mat}, and k''_{cmp} are the second-order dispersion at a pulse stretcher, a material, and a pulse compressor, respectively, and l_{str}, l_{mat}, and l_{cmp} are the

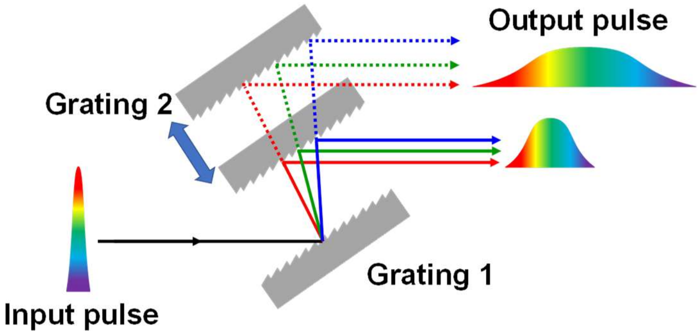

Figure 4.3 | The image of the grating pair as an optical pulse stretcher.

length of each of them. γ_{str} and γ_{cmp} are the incident angles at a pulse stretcher and compressor.

As mentioned above, we can use the grating pair as the compressor and pulse stretcher. In this study, as shown in Fig. 4.3 we use the grating pair as a pulse stretcher to pre-chirp a probe pulse and change the time window of the measurement

4.2.3 Experimental Setup

Figure 4.4 shows a schematic of the optical setup for single-shot pump-probe spectroscopy using photonic time-stretch detection with the CFBG [1]. As a light source, we used a Ti:Sapphire regenerative amplifier system with a pulse duration of 35 fs, center wavelength of 800 nm, and repetition rate of 1 kHz, respectively. The output from the amplifier system entered an optical parametric amplifier (OPA), which generated the signal with a center wavelength of 1300 nm and was utilized as the probe pulse. On the other hand, the residual of the pump pulse in the OPA was used to excite the sample as a pump pulse. The pump pulses are chopped at 500 Hz using an optical chopper, and each probe waveform with a pump pulse is normalized by the average of two probe profiles without the pump just before and after the signal to minimize the influence of the fluctuation of the laser intensity, as shown in Chapter 3. The probe pulse was then pre-chirped by a grating pair (ThorLabs GR50-0613, 600 grooves/mm) and focused on a 1-mm thick zinc telluride (ZnTe) crystal. By simultaneously shining the pump pulse on the sample, pump-probe traces were time-encoded to the spectrum of the chirped probe pulse.

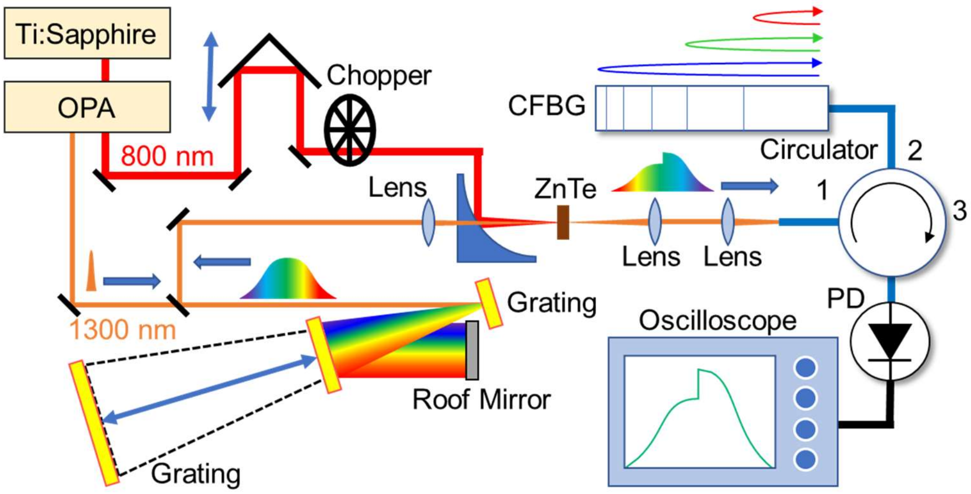

Figure 4.4 | Experimental setup of single-shot pump-probe spectroscopy using photonic time-stretch detection with the CFBG.

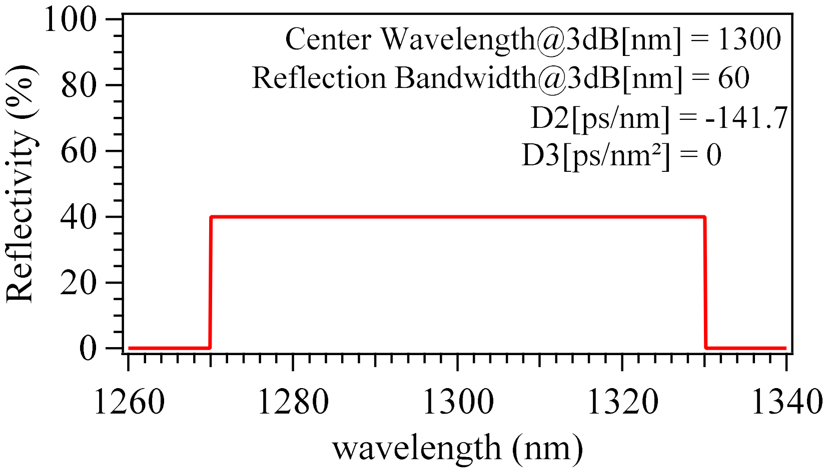

Figure 4.5 | Design of the CFBG reflection wavelength and dispersion parameter D2 and D3 in this study.

The probe pulses were then entered into the CFBG (TeraXion, a center wavelength of reflection and bandwidth were 1300 and 60 nm, respectively, and the designed dispersion parameters were -141.7 ps/nm for D2 and 0 ps/nm^2 for D3, as shown in Figure 4.5) to further extend the encoded probe pulse duration to a nanosecond timescale. The dispersion parameters of the CFBG were designed to apply a large linear chirp without distortion. The reflection from the CFBG was picked up by a polarization-maintaining circulator (ThorLabs CIR1310PM); then the temporal profile after the time stretching was detected by the fast photodiode (PD, ThorLabs DET08C, InGaAs, 5 GHz bandwidth at 800–1700 nm) and recorded using a high-bandwidth real-time oscilloscope (Tektronix DPO712.44C, 12.5 GHz bandwidth, and 100 GS/s sampling rate).

4.3 Results and Discussion

First, we confirmed the pulse extension by the CFBG. Figure 4.6(a) shows the wavelength of the laser pulse from the OPA, which we used in this study. In this condition, the pulse duration broadened from 35 fs to 0.2 ps due to the passage through the OPA. The pulse was transferred through the CFBG to a photodiode, and the observed waveform using an oscilloscope is shown in Figure 4.6(b), which indicates the correspondence between the wavelength of the pulse and pulse duration. The wavelength axis in Figure 4.6(b) is calculated by the dispersion parameters of the CFBG. The edges of the signal appeared at -4 and 4.3 ns, corresponding to the reflection bandwidth of the CFBG, as shown in the gray highlighted area in Fig 4.6(a). The part of the waveform from 4.3 to 8 ns is a signal due to the response of the photodiode, and it can be removed by Fourier filtering

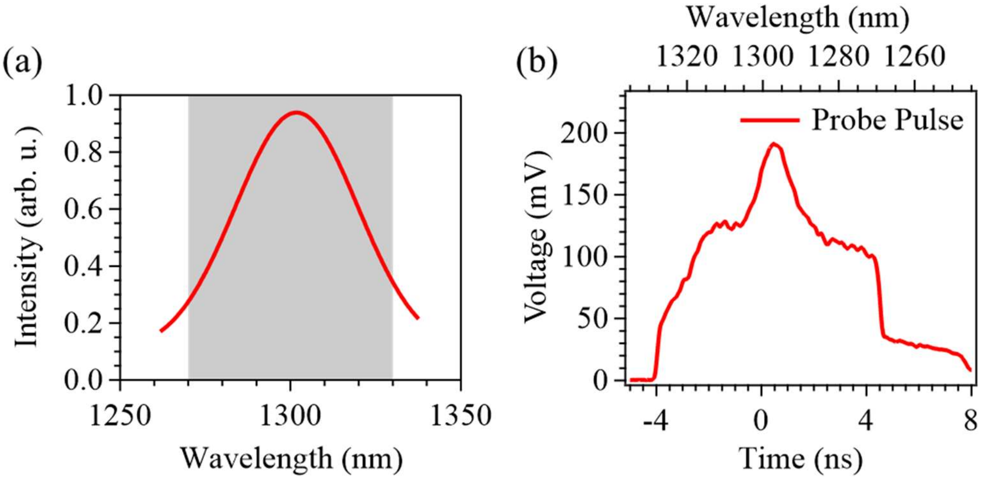

Figure 4.6 | (a) Wavelength of the laser pulse from the OPA. The gray highlighted area is the reflection bandwidth of the CFBG. (b) The observed waveform of the pulse after passing through the CFBG. The corresponding wavelength of the pulse was indicated in the upper axis.

although the filtering was not performed in this study because the effect of the response function of the photodiode was found to be rather small.

By using the high-repetition-rate single-shot measurement method with this CFBG, we measured the pump-probe traces of ZnTe crystal. Figure 4.7(a) shows the typical oscilloscope traces of the probe pulses transmitted through ZnTe with the pump pulse (red dashed line) and without the pump pulse (blue line), which were obtained within a single shot each other. Because the probe pulse was initially negatively chirped at the sample due to the grating pair and was converted to be strongly positive by the CFBG, the time axis of the pump-probe traces was flipped from that in Figure 4.7(b). The horizontal time axis was rescaled to show the pump-probe delay time by moving the delay stage at a certain interval and correcting the

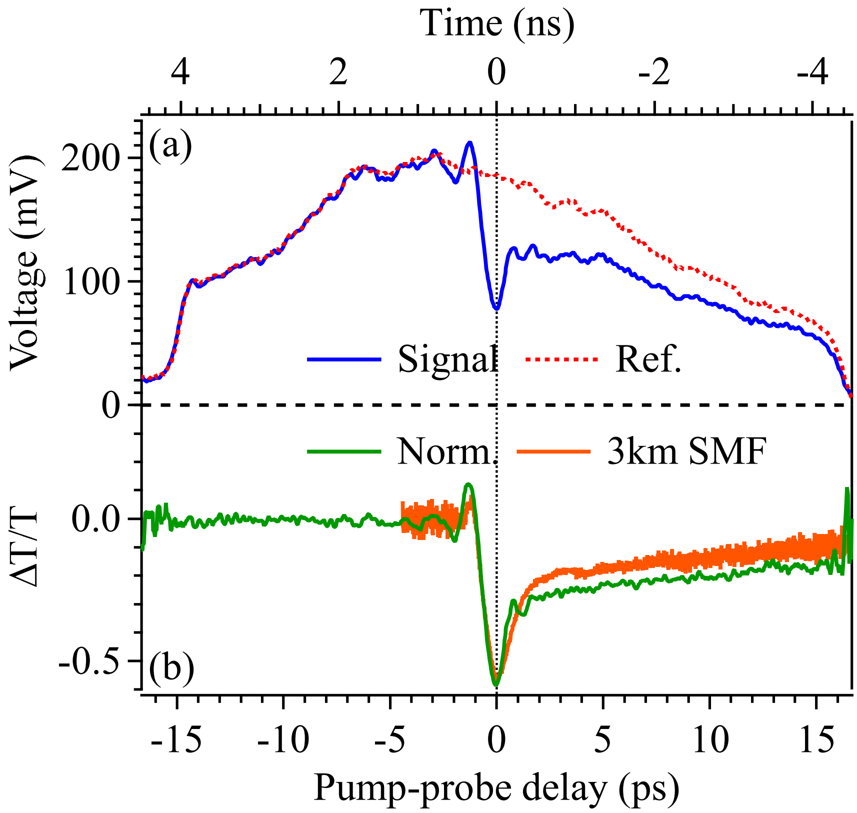

Figure 4.7 | (a) Single-shot oscilloscope traces of the probe pulse with pump pulse (red dashed line) and without the pump pulse (blue line) for ZnTe using the CFBG. (b) Normalized transient transmission changes (ΔT/T) of ZnTe excited at 800 nm calculated from (a) (green line). For comparison, the normalized transient transmission changes of ZnTe probed using the same setup as in Section 3.3 by an 800-nm single-shot pulse and 3-km-long 800-nm single-mode fiber (orange line) are indicated.

timescale from the comparison between the picosecond time delay given by moving the delay stage and the shift of the peak on nanosecond timescale on the oscilloscope. In addition, by scanning the pump-probe delay stage, we confirmed the linear relationship between the time on the oscilloscope (nanoseconds) and the delay time between the pump and probe pulses (picoseconds), and the time window of the obtained pump-probe trace was 30 ps in this case.

The normalized transient transmission change ($\Delta T/T$) calculated from the waveforms in Figure 4.7(a) is shown in Figure 4.7(b). The pump-probe trace of ZnTe via two-photon excitation at 800-nm pump pulse (green line) was observed with a good signal-to-noise ratio, and the decay time agrees well with those obtained in previous reports [16,17]. The noise level of the normalized waveform was $\Delta T/T \sim 0.04$, which was largely improved by our use of the combination of an 800-nm single-shot probe pulse and 3-km-long 800-nm single-mode fiber (SMF, orange line); the noise level of the waveform was $\Delta T/T \sim 0.1$ in the measurement. Even considering the difference in the detecting elements of the photodetectors (InGaAs or Si), this is because the loss of the long optical fiber can be suppressed using the CFBG, and the intensity of the signal detected by the photodiode can be increased.

Next, to demonstrate the variable time window using a grating pair, we changed the distance of the grating pair and then measured the waveforms of the transient transmittance change of ZnTe. Figure 4.8(a) shows the pulse duration of the probe

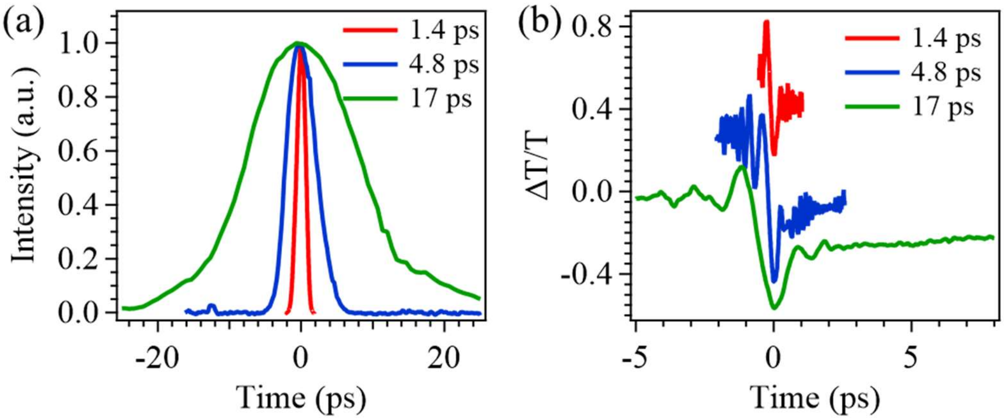

Figure 4.8 | Pump-probe measurements of ZnTe by changing the time window. (a) Second-harmonic autocorrelation of the probe pulses for different positions of the grating pair. (b) Transient transmission changes of ZnTe observed with the same condition for probe pulses as in (a).

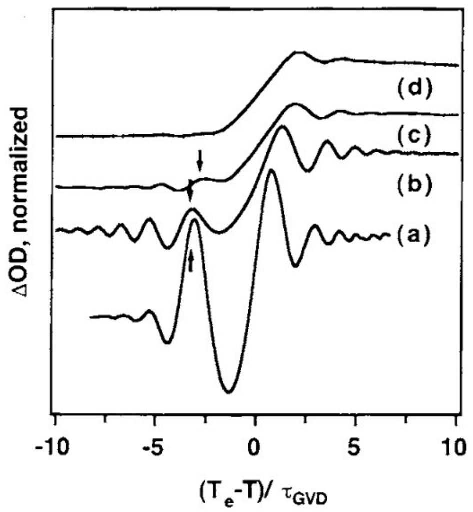

Figure 4.9 | Differences in the waveform distortion when the same signal was detected by different amounts of dispersion in the probe pulses [18].

pulses measured by autocorrelation using a BaB_2O_4 (BBO) crystal for different distances of the grating pair. The durations of the probe pulses were 1.4 (red line), 4.8 (blue line), and 17 ps (green line) at FWHM, respectively. In the case of single-shot spectroscopy using these chirped pulses, the time resolution of the probe pulse depends on the pulse duration, as shown in Eq. (2.2.6) in Section 2.2, where τ_0 and τ_c represent the pulse duration of transform-limited (80 fs) and chirped pulses, respectively. The time resolutions of the single-shot measurements using these pulses were then calculated to be 0.33 (red line), 0.62 (blue line), and 1.2 ps (green line), respectively. The measured transient transmission changes of ZnTe are shown in Figure 4.8(b). The peak-to-peak rise time near 0 ps agrees with the calculated time resolution, which indicates the validity of our setup. Importantly, some fringes were observed around the time origin in these waveforms in Figure 4.8(b). These may be due to the inevitable distortion of the waveforms in the time-encoding technique, and we obtained the same trend observed in Ref. [18].

Finally, to demonstrate the simultaneous observation of ultrafast dynamics and slow changes, we measured the transient transmittance changes of ZnTe within 1 second while rapidly changing the pump-probe delay time by moving the computer-controlled delay stage. Figure 4.10(a) shows the resultant 2D array of 500 traces. Since the pump pulses were chopped at 500 Hz, we obtained the pump-probe traces at every 2 ms. From the 80th frame to the 400th frame, which corresponds to 0.64 s, the peak of the transient transmittance change shifted as the number of frames

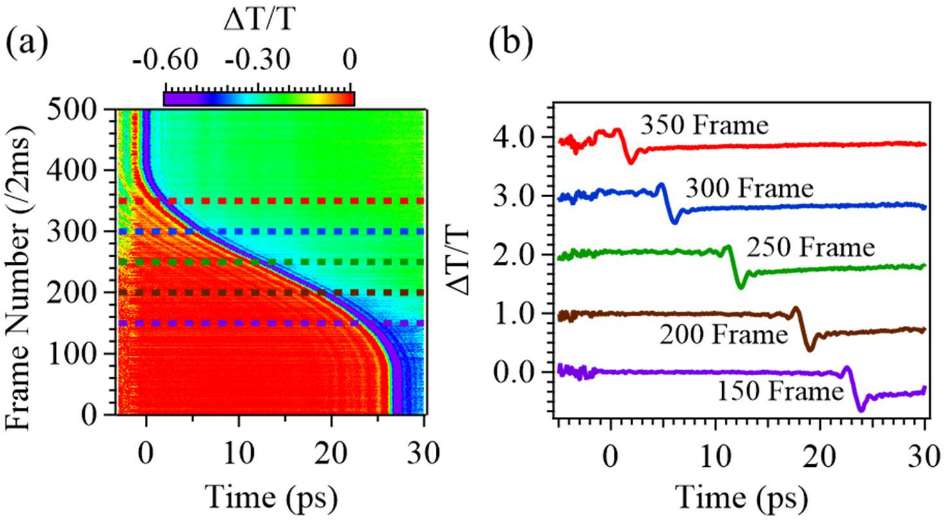

Figure 4.10 | (a) Fast-frame acquisition of transient transmission changes in ZnTe. The delay stage of the pump pulse was moved by 4 mm (i.e., 27 ps in delay time) in 1 second to rapidly change the pump-probe delay time. The vertical axis corresponds to the frame number of each shot that repeats at 500 Hz. The pulse duration of the probe pulse at the sample was 17 ps. (b) Waveforms of the transient transmittance change at five locations, 150, 200, 250, 300, and 350 frames, indicated by the broken dashed lines in (a).

increased. The slices of the contour plot in Figure 4.11(a) at 150th, 200th, 250th, 300th, and 350th frames are shown in Figure 4.10(b). Since these waveforms are quite similar, the results indicate the precise measurement of transient transmittance throughout the time window and the lack of waveform distortion in the time direction because of the linear chirp of the CFBG.

4.5 Conclusion in Chapter 4

In conclusion, we have demonstrated a high-repetition-rate single-shot method using a CFBG and grating pair. By using a CFBG to temporally stretch the spectrum, the signal-to-noise ratio of the probe pulses was dramatically improved compared with the case of using a long optical fiber. The variable time window of the measurement was demonstrated using a grating pair, and it allowed us to extend the scale of observable phenomena and materials.

References

[1] M. Kobayashi, Y. Arashida, G. Yamashita, E. Matsubara, M. Ashida, J. A. Johnson, and I. Katayama, “Fast-frame single-shot pump-probe spectroscopy with chirped-fiber-Bragg gratings,” Opt. Lett. 44, 163 (2019).

[2] R. Kashyap, “Fiber Bragg gratings, 2nd edition,” Academic Press (2010)

[3] T. Erdogan, “Fiber grating spectra,” J. Light. Technol. 15, 1277 (1997).

[4] K. O. Hill and G. Meltz, “Fiber Bragg grating technology fundamentals and overview,” J. Light. Technol. 15, 1263 (1997).

[5] G. Palumbo, D. Tosi, A. Iadicicco, and S. Campopiano, “Analysis and design of chirped fiber Bragg grating for temperature sensing for possible biomedical applications,” IEEE Photonics J. 10, 1 (2018).

[6] J. Zhang and J. Yao, “Broadband microwave signal processing based on photonic dispersive delay lines,” IEEE Trans. Microw. Theory Tech. 65, 1891 (2017).

[7] F. Ouellette, “Fiber Bragg gratings help WDM push limits of fiber capacity,” Laser Focus World 34, 3, 83 (1998).

[8] P. Bettini, E. Guerreschi, and G. Sala, “Development and experimental validation of a numerical tool for structural health and usage monitoring systems based on chirped grating sensors,” Sensors (Basel, Switzerland) 15, 1, 1321 (2015).

[9] Y. Okabe, R. Tsuji, and N. Takeda, “Application of chirped fiber Bragg grating sensors for identification of crack locations in composites,” Compos. Part A Appl. Sci. Manuf. 35, 1, 59 (2004).

[10] O. Ogawa, “Chromatic dispersion in optical fibers and its compensation technology,” T. IEE Japan 122-C, 4 (2002)

[11] C. Rullière, “Femtosecond laser pulses principles and experiments second edition,” Springer (2005).

[12] P. Maine, D. Strickland, P. Bado, M. Pessot, and G. Mourou, ‘‘Generation of ultrahigh peak power pulses by chirped pulse amplification,’’ IEEE J. Quantum Electron. 24, 398 (1988).

[13] B. E. Lemoff and C. P. J. Barty, ‘‘Quintic-phase-limited, spatially uniform expansion and recompression of ultrashort optical pulses,’’ Opt. Lett. 18, 1651 (1993).

[14] W. E. White, F. G. Patterson, R. L. Combs, D. F. Price, and R. L. Shepherd, ‘‘Compensation of higher-order frequency dependent phase terms in chirped-pulse amplification systems,’’ Opt. Lett. 18, 1343 (1993).

[15] S. Kane and J. Squier, “Grism-pair stretcher-compressor system for simultaneous second- and third-order dispersion compensation in chirped-pulse amplification,” J. Opt. Soc. Am. B 14, 3, 661 (1997).

[16] E. Ghahramani, D. J. Moss, and J. E. Sipe, “Full-band-structure calculation of first-, second-, and third-harmonic optical response coefficients of ZnSe, ZnTe, and CdTe,” Phys. Rev. B 43, 9700 (1991).

[17] M. Schall and P. U. Jepsen, “Above-band gap two-photon absorption and its influence on ultrafast carrier dynamics in ZnTe and CdTe,” Appl. Phys. Lett. 80, 4771 (2002).

[18] I. A. Shkrob, D. A. Oulianov, R. A. Crowell, and S. Pommeret, “Frequency-domain “single-shot” ultrafast transient absorption spectroscopy using chirped laser pulses,” J. Appl. Phys. **96,** 25 (2004).

Chapter 4

Chapter 5

Multiscale Dynamics under High-Density Photoexcitation

5.1 Introduction

In the previous chapters, we have demonstrated a high-repetition single-shot measurement method and increased its sensitivity. These results have enabled us to apply our method to investigate multi-timescale and pulse-to-pulse dynamics of irreversible and complex phenomena, such as photoinduced phase change [1-4], surface modification, and laser ablation [5-10], which were introduced by the cooperative changes in the atomic arrangement of materials due to high-density excited states. These phenomena are fundamentally important in that optical excitations lead to energy relaxations on a multi-timescale, as a result, the dynamics of pulse-to-pulse changes may occur, such as the incubation effect in laser processing [12-15] and formation of LIPSS [5,16-19]. Understanding the mechanisms of these phenomena is important for not only enhancing our fundamental understanding but also exploiting and controlling them for novel applications.

One of the most interesting materials to study pulse-to-pulse dynamics under high-density photoexcitation is $Ge_2Sb_2Te_5$ (GST) thin films [20-23]. Using our high-repetition-rate single-shot spectroscopy with CFBG, we investigated the ultrafast dynamics at each step in a series of photoinduced irreversible events, including the photoinduced phase change from the crystalline phase to the amorphous phase and the subsequent pulse-to-pulse LIPSS formation in GST films.

5.2 Experimental Methods

5.2.1 Laser-Induced Periodic Surface Structures (LIPSS)

Recently, laser processing technologies using ultrashort pulsed lasers have been extensively investigated in many fields [5-10]. Among them, LIPSS involves periodic nanoscale structures induced by laser pulse irradiation near the ablation threshold [5,16-19]. LIPSS is attracting attention as one of the next-generation nanofabrication technologies and can be used for friction reduction [24], spatially

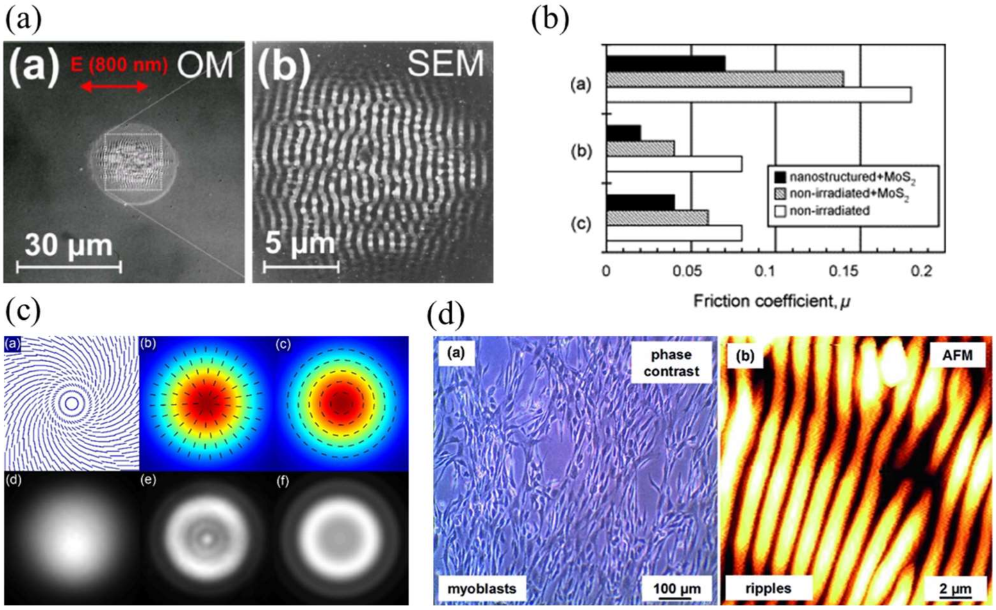

Figure 5.1 | Examples of applications of LIPSS formation. (a) SEM image of LIPSS on a Si wafer surface [29]. (b) Difference in friction reduction with and without LIPSS formation on a diamond-like carbon film [24]. (c) Spatially distributed wave plate [10]. (d) Cell extension control of human myoblasts on LIPSSs on polystyrene [25]. Adapted from: (a)–Ref. [29], (b)–Ref. [24], (c)–Ref. [10], and (d)–Ref. [25].

distributed wave plates [10], and cell extension control [25,26]. LIPSS was first observed by Birnbaum [5] on various semiconductor surfaces in 1965; then, many examples were reported in a variety of materials [16-18,27]. Studying LIPSS formation, however, is very difficult because many parameters such as irradiation laser wavelength, pulse width, fluence, polarization state, pulse repetition, sample surface state, and material type can critically affect the formation of the periodic structures.

It is known that LIPSSs were typically formed by the excitation of surface plasmon polaritons and the interaction between incident laser pulses and electromagnetic waves scattered on the sample surface [28-31]. However, it is necessary to understand feedback processes between laser irradiations because topographical, structural, or chemical changes induced by a pump laser pulse can accelerate or decelerate LIPPS formation in subsequent laser pulses [28,32]. In addition, pronounced LIPSS can be formed by multiple laser pulse irradiations, suggesting the importance of inter-pulse interactions. Therefore, temporal dynamics associated with surface structural changes due to LIPSS formation, especially during multiple laser pulse irradiations, need to be clarified.

However, the conventional pump-probe measurement used for investigating ultrafast dynamics is difficult to study LIPPS formation since it requires collecting multiple measurements under the same conditions, whereas LIPPS formation involves irreversible structural changes on the sample surface with each laser shot.

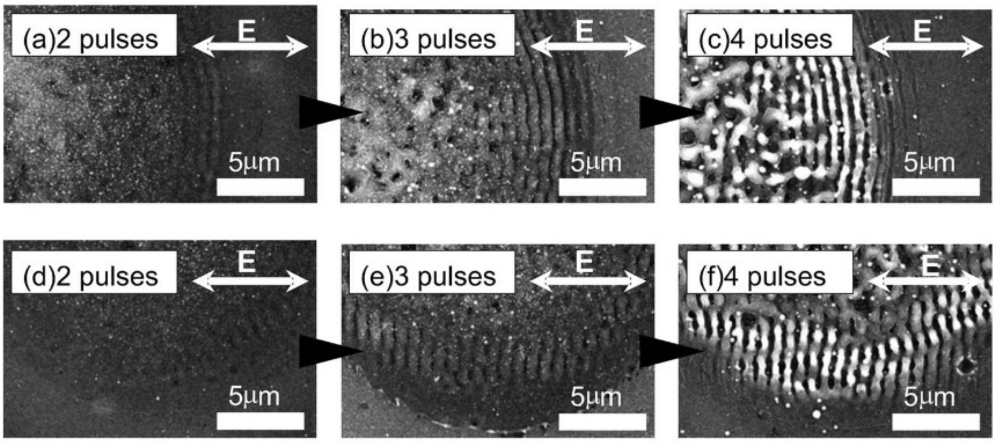

Figure 5.2 | Laser pulse number-dependent development of surface wave structures [32]. Adapted from Ref. [32].

Therefore, using our high-repetition-rate single-shot method, we investigated the pulse-to-pulse dynamics during LIPSS formation on a GST film.

5.2.2 Characteristics of $Ge_2Sb_2Te_5$ (GST)

GST is one of the Te-based chalcogenide alloys that exhibit phase change between crystalline and amorphous phases [20-23] and is used as a medium for optical media disks, such as CDs and DVDs, and non-volatile electronic memory (PCRAM) due to the large difference in optical constants and repeatable switching between two phases [33-35].

GST is metastable and has a face-centered cubic (fcc) structure at low temperatures, while it is stable and has a hexagonal (hex) structure at high temperatures [36]. Figure 5.3 shows the crystal structure of GST. The atoms are mainly bound to each other by p-electrons (Ge: $4s^2 4p^2$, Sb: $5s^{2.4}p^3$, Te: $5s^{2.4}p^4$) and

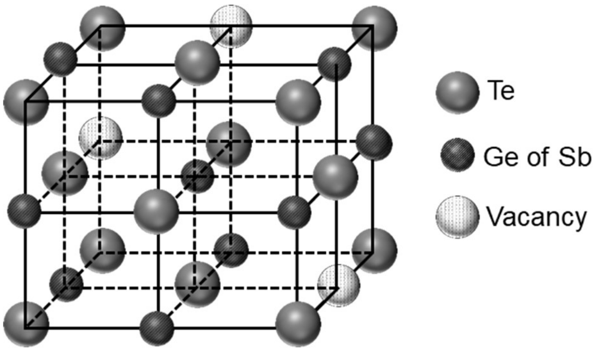

Figure 5.3 | Crystal structure of GST [36].

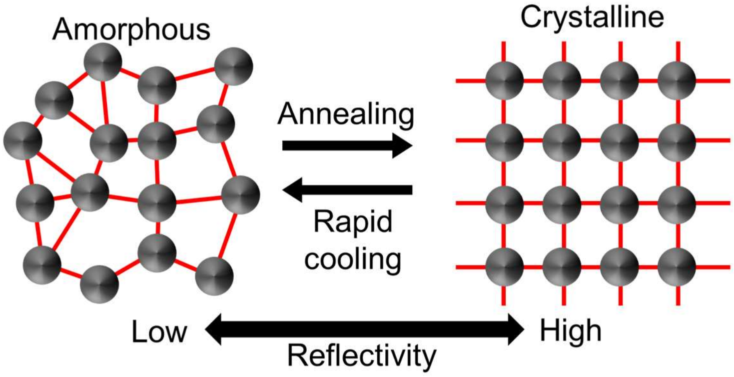

Figure 5.4 | Thermally induced phase change between the crystalline and amorphous phases using nanosecond laser pulses.

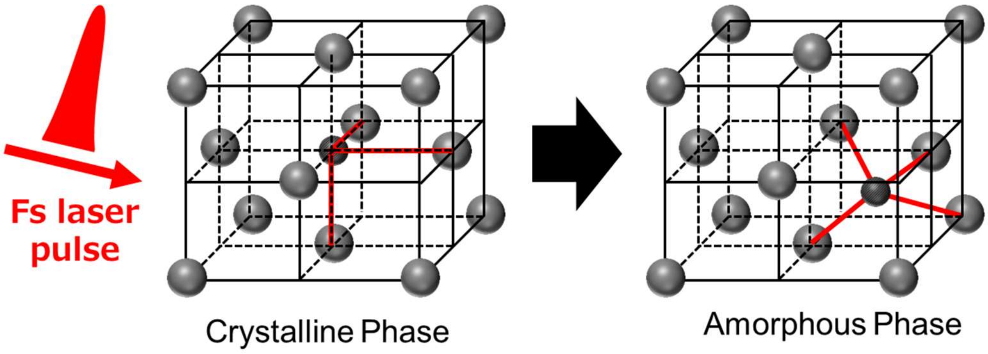

Figure 5.5 | Non-thermal phase change from the crystalline to the amorphous phase using ultrashort laser pulses.

are equidistant with 6 neighboring atoms, and the coordinating atoms form an octahedron.

In optical media disks, a nanosecond-pulse laser is used to thermally induce a phase change between the two phases, as shown in Fig. 5.4. When recording some information to the optical disk, nanosecond laser pulses are irradiated at high power to induce a phase change from the crystalline to the amorphous phase. The irradiated area is instantly heated above the melting point (600-700 ℃) and then rapidly cooled to form a recording mark of the amorphous phase. On the contrary, to erase the recorded information, amorphous marks are crystallized by raising the temperature to ~400-500 ℃ using a relatively weak laser power [37]. This process induces a thermal phase change and is completed in tens of nanoseconds.

Recently, the ultrafast non-thermal phase change from the crystalline to the amorphous phase has been demonstrated using femtosecond-to-picosecond ultrashort laser pulses [4,38-40]. In this non-thermal process, the phase change is completed without the liquid phase. Figure 5.5 shows a conceptual model of the structural change with non-thermal amorphization of GST [41,42]. By femtosecond laser irradiation, the Ge-Te resonant bond is broken by the excitation of electrons relatively weakly bound between the Ge and Te atoms into anti-bonding orbitals. In this case, amorphization occurs due to the displacement of the Ge atom from 6 to 4 coordination. First-principles simulations also show the importance of excited electrons in the amorphization of GST, and according to the simulations, the amorphous phase of GST with electronic excitations can be taken as a disordered state with a mixture of various local structures [43].

Furthermore, surface processing of GST thin films using ultrashort laser pulses has been studied to reveal the dynamics of LIPSS formation. Several groups reported LIPSS formation on GST [44,45], but its dynamics have not been fully understood using the conventional pump-probe spectroscopy. Thus, we utilized our high-repetition-rate single-shot method with a CFBG to reveal the ultrafast multi-timescale dynamics of each step in a series of photoinduced irreversible events in the time domain from photoinduced phase change (crystalline to amorphous phase) to subsequent pulse-to-pulse LIPSS formation in highly excited GST thin films.

5.2.3 Experimental Setup

Figure 5.6 shows the schematic of the experimental setup for high-repetition-rate single-shot pump-probe spectroscopy with a CFBG. We used Yb:KGW regenerative amplifier system (pulse duration: 290 fs, center wavelength: 1028 nm, repetition rate: 75 kHz). The part of the output from the amplifier system pumped the OPA to generate 1300-nm probe pulses, and the rest of the amplifier output was used as pump pulses; both wavelengths were expected to induce a large change in optical constants with the crystalline-to-amorphous phase transition of GST. The repetition of the pump was reduced to 15 kHz using an acousto-optic modulator

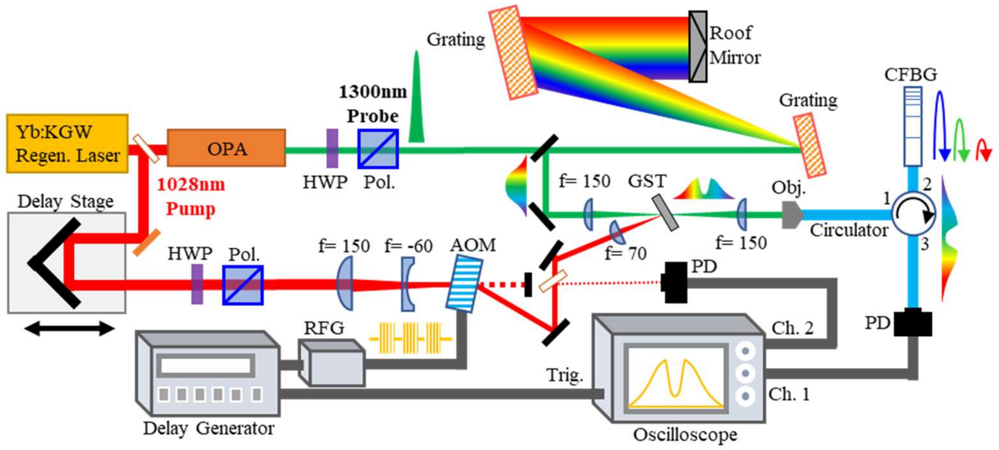

Figure 5.6 | Experimental setup of the single-shot pump-probe spectroscopy using photonic time-stretch detection with a CFBG. HWP: half-wave plate, Pol.: polarizer, AOM: acousto-optic modulator, Obj.: objective lens, PD: photodiode, RFG: radio frequency generator, Trig.: trigger signal channel.

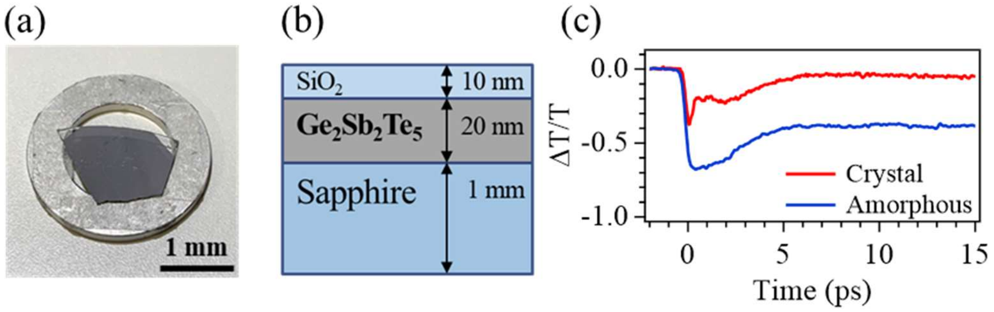

Figure 5.7 | (a) GST used in this work. (b) Cross-sectional image of the GST film. GST film with a thickness of 20 nm was deposited on a sapphire substrate and covered with a 10-nm-thick SiO_2 protection layer. (c) Transient transmittance changes in the crystalline and amorphous phases of GST using conventional pump-probe spectroscopy.

(AOM). The probe pulse was chirped by a grating pair to encode the ~30 picosecond photoinduced time profile and shined on GST. The transient transmittance passing through the GST film was measured on a single-shot basis with the time-encoding technique, and then, the time profile of the probe was obtained with the time-stretch method using a CFBG, as shown in Chapter 4. To tune the number of pump pulses as well as synchronize the timing of waveform acquisition, an AOM and a delay generator (Stanford Research Systems DG645) were introduced into the system. The repetition rate of the pump pulse was then reduced to 15 kHz, and the transient transmittance was calculated from the ratio of the transmittance profiles with and without the pump pulse. Eventually, 15000 pump-probe traces were obtained per second with a good signal-to-noise ratio. After implementing each set of spectroscopic measurements, we confirmed the laser-induced modification of the surface structure using a laser microscope (Keyence VK-X1100) with a wavelength of 404 nm and a numerical aperture of 0.95.

Figure 5.7(a) shows the photo of the GST film used in this work. The 20-nm thick GST film was deposited on a sapphire substrate using high-frequency magnetron sputtering and covered with a 10-nm-thick SiO_2 protection layer (Figure 5.7(b)). This sample was annealed for 15 min at 250 °C to produce an fcc crystalline phase. Figure 5.7(c) shows the measured transient transmittance change of the crystalline phase and the amorphous phase of the GST film below the phase change threshold with conventional pump-probe spectroscopy. The result clearly shows the difference in the relaxation times of the photoexcited states in the crystalline and amorphous phases (3.2 ps and ~200 ps at 1300 nm, respectively). The relaxation times of the transient transmittance change were different from those reported in previous works [4,46], possibly because of the difference in the excitation and probed wavelengths.

5.3 Results and Discussion

First, we measured the surface structure and ultrafast transient response of GST with different excitation densities. Figures 5.8(a)-(d) show the microscopic surface images of GST films after the irradiation of 400 pulses at different pump fluences. The red broken circles indicate the irradiation spot of the probe pulses with 30-μm diameter. The pump fluences were classified into three groups: below the threshold excitation fluences for the crystalline-to-amorphous phase change (9.8 mJ/cm^2), the excitation fluences capable of the amorphization but incapable of LIPPS formation (22 mJ/cm^2), and the excitation fluences capable of LIPPS formation but incapable of ablation (25 and 29 mJ/cm^2). The corresponding pump-probe traces as a function of the pump laser shot were plotted in a 2D image, as shown in Figs. 5.8(e)-(h). The transmittance change is represented by a color scale. Several waveforms extracted from the images are also shown.

When the pump fluence (9.8 mJ/cm^2) is lower than the amorphization density, the microscopic image shows almost uniform change or no change in the surface (Figure 5.8(a)). According to this result, the pump-probe traces are almost the same in each pump laser shot (Figs. 5.8(e)), whose transient behavior represents the dynamics in the crystalline phase. The transient transmittance relaxes to almost zero within 5 ps, which is consistent with that obtained by conventional pump-probe measurements, as shown in Figure 5.7(c); however, the waveforms were distorted near the time origin by the artifact of the single-shot detection method with chirped pulses, as mentioned in Chapter 4 [47].

In the case of a pump fluence of 22 mJ/cm^2, the pump pulse optically induces the crystalline-to-amorphous phase change. As shown in the microscopic image in Figure 5.7(b), the pump-irradiated part of the crystalline phase (light gray) changes

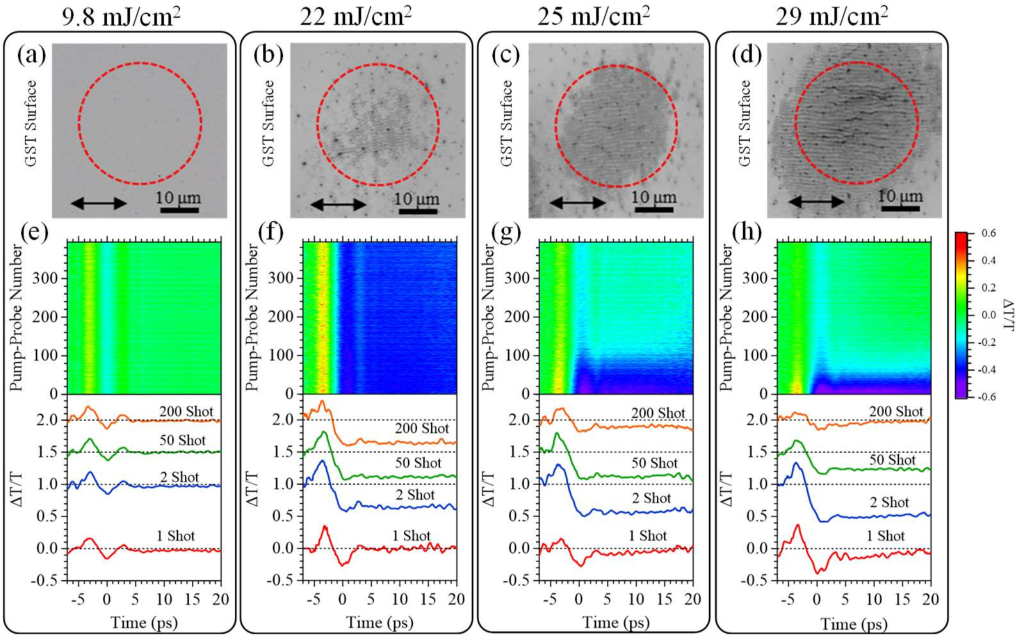

Figure 5.8 | (a)-(d) Microscopic images of GST after the irradiation of 400 pulses at different pump fluences. Arrows indicate the polarizations of the pump pulses. (e)-(h) The pump-probe ultrafast traces for each pump laser shot plotted in a 2D color image (upper column). Vertical axis is the number of pump-probe number, and the horizontal axis is the pump-probe delay time. Several pump-probe waveforms extracted from the 2D color images (bottom column).

to the amorphous phase (dark gray) after 400 pump laser shots. Corresponding to this change, the 2D image (Figure 5.7(f)) also shows an apparent contrast in color near the time origin. The transient transmittance of the first pulse agrees with that in the crystalline phase (Figure 5.7(e)), while that observed in the later pump pulses (> 2 shot) shows a slower relaxation that takes more than 20 ps, which is the time window of the probe pulses. This difference in the pump-probe traces between the first shot and later shots manifests the difference in relaxation dynamics between the crystalline and amorphous phases in GST.

In the cases of pump fluences of 25 mJ/cm^2 and 29 mJ/cm^2, the microscopic image shows a periodic surface structure formed in the amorphous phase, which is the fingerprint of LIPSSs (Figs. 5.7(c) and 5.7(d)). The LIPSSs with approximately 1-μm periodicity were arranged parallel to the polarization direction of the pump pulses (solid arrows), whose characteristics are consistent with that in the previous research [44,45]. In this case, the LIPSS is classified as the low-spatial-frequency

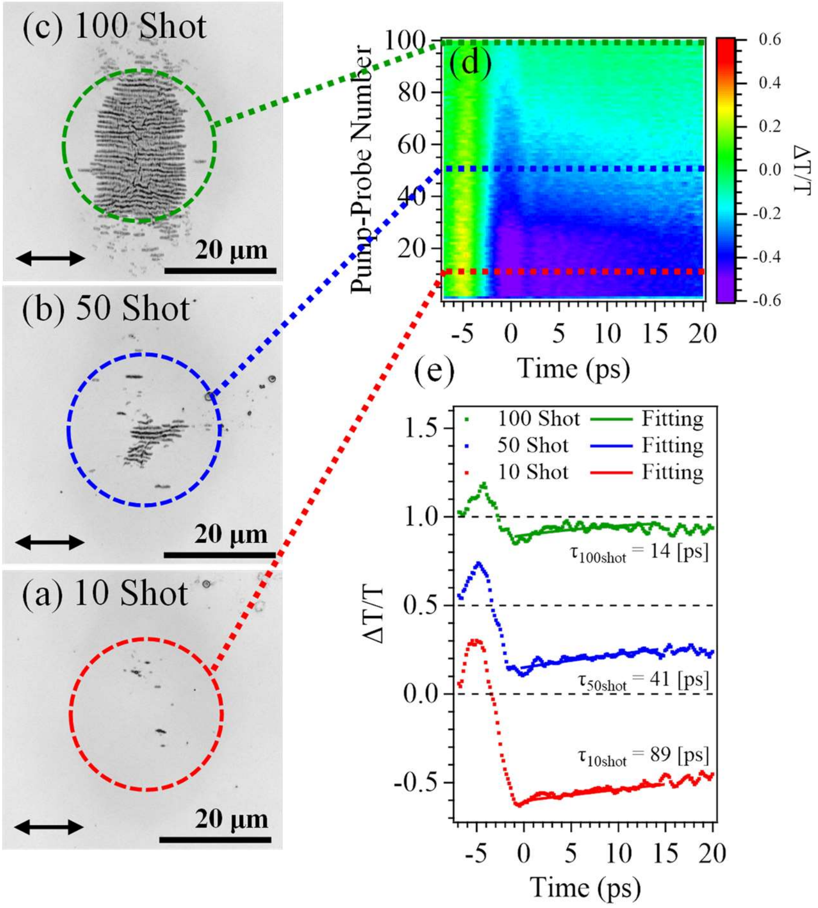

Figure 5.9 | (a)-(c) Microscopic images of the laser-induced spot of GST after pump irradiations of 10, 50, and 100 pulses at pump fluence of 29 mJ/cm^2. Each image was obtained at a different location of the same GST sample, and the red broken lines indicate the spot of the probe pulses. The inserted arrows in microscopic images indicate the polarization directions of the pump pulses. (d) Corresponding transient transmittance change for 100 pump laser shot plotted in a 2D color image (upper panel). The transient transmittance waveforms and exponential fittings at 10, 50, and 100 shots indicated by the broken lines in 2D color image (bottom panel).

LIPSS type-II (LSFL-II) reported in Ref. [28] because the grooves are formed with a periodicity comparable to the wavelength of the pump pulse and arranged parallel to the pump polarization. LSFL-II is generally observed on the dielectrics when the single photon energy of the pump pulse is smaller than the bandgap energy of the materials. The origin of the LFFL-II is related to radiation remnants [28]. The reasons for the formation of LSFL-II on GST could be due to the modulation of bandgap by thin film of the GST. Notably, the 2D images of the transient transmittance change shown in Figs. 5.7(g) and 5.7(h) significantly depend on the number of the pump pulse, in contrast to the images where no LIPSS is formed (Figs. 5.7(e) and 5.7(f)). As shown in Figs. 5.7 (g) and 5.7 (h), the pump-probe trances in the first and second shots are similar to those in the case of 22 mJ/cm^2, indicating that they correspond to the dynamics in the crystalline and amorphous phases, respectively. However, as the number of pump-pulse irradiations increases, the amplitude and relaxation time of the transient transmittance changes tended to decrease. Furthermore, as displayed in Figs. 5.7(h), the decreasing trend occurs more quickly at an excitation density of 29 mJ/cm^2.

To further clarify the step-by-step surface modification dynamics during LIPSS formation, we measured the microscopic images of the GST thin film after irradiations of 10, 50, and 100 pump pulses with a pump fluence of 29 mJ/cm^2 (Figs. 5.9(a)-(c)) and compared them with the corresponding pump-probe dataset (Figs. 5.9 (d)). The images taken at different locations on the same GST film show that LIPSSs gradually grow on the amorphous phase as the number of the pump irradiation increases. Correspondingly, the relaxation time of the pump-probe traces gradually becomes faster, which is visible after ~40 pump laser shots. To analyze the observed step-by-step relaxation dynamics, we estimated the relaxation time of each transient transmittance change using a simple exponential function:

$$f(t) = -C \exp(-t/\tau_n). \tag{5.3.1}$$

Here, C and τ_n indicate the amplitude and relaxation time of the transient transmittance change, respectively. Using this fitting procedure, the relaxation times for 10, 50, and 100 shots were estimated as 89 ps, 41 ps, and 19 ps, respectively, as shown by the solid curves in Figure 5.9(d). These results show that changes in the pulse-to-pulse ultrafast dynamics are associated with the step-by-step surface modification or LIPSS formation.

To examine the transition of the pump-probe response, Figure 5.10 summarizes the results of the pulse-to-pulse changes in the relaxation time and amplitude of the transient transmittance change, as well as the transmitted probe intensity in the case of 22, 25, and 29 mJ/cm^2 pump fluences. The overall dynamics can be classified into three regions: (I) the region where GST is crystalline (light gray), (II) the region where GST is amorphous (light blue), and (III) the region that involves LIPSS (light yellow).

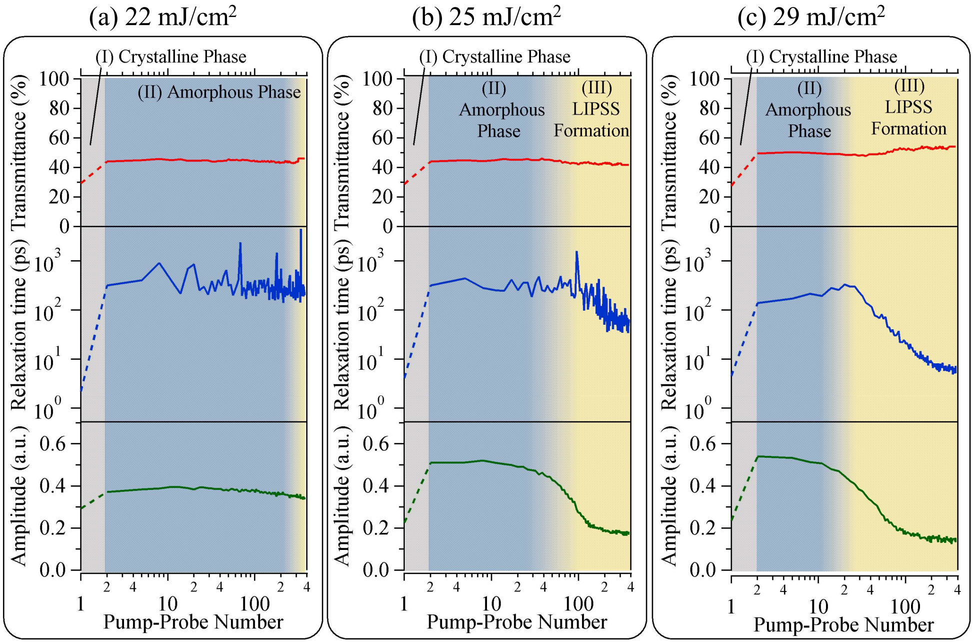

Figure 5.10 | Transmittance of reference pulses (top), the relaxation time of the transient transmittance change (middle), and the amplitude changes of the transient transmittance change (bottom). These data were obtained at pump fluences of (a) 22, (b) 25, and (c) 29 mJ/cm^2.

When the pump fluence is 22 mJ/cm^2 (Figure 5.10(a)), the first pump pulse induces the amorphization, and the increase in the relaxation time and the amplitude of the transmittance change follow along with the phase change. Then, after the second pump pulse, in region (II), the transmitted probe intensity, relaxation time, and amplitude are almost constant. On the other hand, in the case of 29 mJ/cm^2 pump fluence shown in Figure 5.10(c), the amorphization is induced by the first pump pulse in region (I), as for 22 mJ/cm^2 pump fluence. Then, in region (II), the relaxation time is almost constant until the 25th shot, implying that the GST film holds the amorphous phase without an apparent LIPSS formation, and thus, similar dynamics can be observed (Figs. 5.9(a) and 5.9(d)). In region (III) where the step-by-step LIPSS formation takes place, the relaxation time and amplitude gradually decrease as the number of pump pulse irradiations increases. After the irradiation of ~200 pump laser shots, the LIPSS formation is eventually completed, and the values are close to constant. In the case of 25 mJ/cm^2 pump fluence (Figure 5.10 (b)), the transition from region (II) to (III) starts slower than that of 29 mJ/cm^2.

Next, we focus on the mechanism of why the relaxation time decreases during LIPSS formation. It is reported that LIPSS is easily formed by the presence of defects, impurities, or rough spots on the sample surface [28]. Figure 5.9(a) and 5.9(b) also show this trend. In addition, cascading of carrier generations (avalanche effect) originated from the nonlinear process such as the impact ionization might contribute to macroscopic groove formation deeply inside the sample [48]. Based on the observed experimental results, as shown in Figure 5.11, we propose a possible scenario for the overall dynamics of LIPSS formation. The first pump pulse induces the phase change from the crystalline to the amorphous phase. Accordingly, the scattering of invisible defects, impurities, or rough spots, which acts as a trigger for the initial LIPSS formation, is formed inside the pump excitation area (region (I) in Figure 5.10).

Subsequently, the following 2-15 pump laser shots at 29 mJ/cm^2 excitation raise the number of defects, impurities, or rough spots, and some of them become visible due to their accumulation, as shown in Figure 5.9(a). During this stage, similar dynamics can be observed in the amorphous phase (region (II) in Figure 5.10(b) and 5.10(c)), while the triggers of LIPPS formation gradually increase. Then, further irradiation with pump laser shots causes excess photoexcited carriers and their cascading, which can yield the deformation of the surface structure around

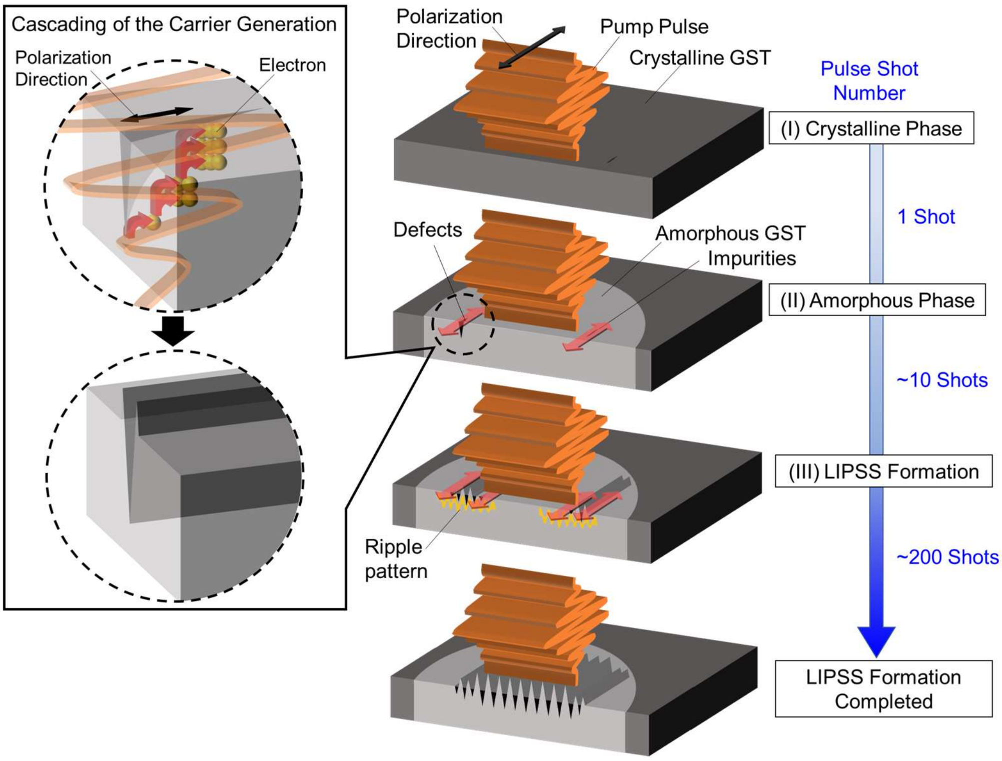

Figure 5.11 | Schematic of LIPPS formation dynamics in GST.

defects, impurities, or rough spots, leading to the local formation of small groove structures parallel to the polarization of pump laser pulses. Once the local groove structures are formed, the number of defects, impurities, and rough spots exponentially increases, decreasing both the relaxation time and the amplitude of transient transmittance. Scattering of the pump pulses and the accelerated relaxation convert the excess energy from photoexcited carriers to structural deformation. This stage corresponds to region (III). Comparing the application of 25 mJ/cm^2 versus 29 mJ/cm^2 pump fluence (Figure 5.10), we deduce that this effect seems to be accelerated, depending on the pump fluence.

The scattering around the groove structures can also induce a ripple pattern due to the interference between scattered laser fields, whose periodicity is almost the same as the pump wavelength. Finally, the energy input into the local groove structures provided from multiple pump laser shots facilitates the macroscopic LIPSS formation (Figure 5.9(c)). Although a sophisticated model that can quantitatively explain LIPSS formation dynamics is still required, our high-repetition-rate single-shot pump-probe spectroscopy enables us to reveal the pulse-to-pulse ultrafast dynamics from the initial excited state to LIPPS formation or laser ablation via the crystalline-to-amorphous phase change in GST films.

5.4 Conclusion in Chapter 5

In conclusion, we have demonstrated the observation of pulse-to-pulse dynamics from the initial photoexcitation to LIPSS formation and laser ablation via the crystalline-to-amorphous phase change in GST thin films. We found that the relaxation time and the amplitude of the transient transmittance change during LIPSS formation decrease with increasing pump laser shots. The results indicate that LIPPS formation is triggered by nucleation around defects, impurities, or rough spots, and the resultant efficient and ultrafast relaxation of excited states around them gradually forms periodic structures possibly due to carrier multiplications and subsequent energy relaxations that cause structural deformation.

References

[1] S. Koshihara, Y. Tokura, K. Takeda, and T. Koda, “Reversible photoinduced phase transitions in single crystals of polydiacetylenes,” Phys. Rev. Lett. **68,** 1148 (1992)

[2] T. Tayagaki and K. Tanaka, “Photoinduced phase transition to a new macroscopic spin-crossover-complex phase,” Phys. Rev. Lett. **86,** 2886 (2001)

[3] T. Taniguchi, H. Sato, Y. Hagiwara, T. Asahi and H. Koshima, “Photo-triggered phase transition of a crystal,” Commun. Chem. **2,** 19 (2019).

[4] M. Hada, W. Oba, M. Kuwahara, I. Katayama, T. Saiki, J. Takeda, K. G. Nakamura, “Ultrafast time-resolved electron diffraction revealing the nonthermal dynamics of near-UV photoexcitation-induced amorphization in $Ge_2Sb_2Te_5$,” Sci. Rep. **5,** 13530 (2015).

[5] M. Birnbaum, “Semiconductor surface damage produced by ruby lasers,” J. Appl. Phys. **36,** 3688 (1965).

[6] Z. Guosheng, P. M. Fauchet, and A. E. Siegman, “Growth of spontaneous periodic surface structures on solids during laser illumination,” Phys. Rev. B **26,** 5366 (1982).

[7] C. Momma, B. N. Chichkov, S. Nolte, F. Von Alvensleben, A. Tünnermann, H. Welling, and B. Wellegehausen, “Short-pulse laser ablation of solid targets,” Opt. Commun. **129,** 134 (1996).

[8] G. Dumitru, V. Romano, H. Weber, M. Sentis and W. Marine, “Femtosecond ablation of ultrahard materials,” Appl. Phys. A **74,** 729 (2002).

[9] K. Sugioka, “Progress in ultrafast laser processing and future prospects,” Nanophotonics **6,** 393 (2017).

[10] M. Beresna, M. Gecevičius, P. G. Kazansky, and T. Gertus, “Radially polarized optical vortex converter created by femtosecond laser nanostructuring of glass,” Appl. Phys. Lett. **98,** 1 (2011).

[11] K. C. Phillips, H. H. Gandhi, E. Mazur, and S. K. Sundaram, “Ultrafast laser processing of materials: a review,” Adv. Opt. Photon. **7,** 684 (2015)

[12] M. Lenzner, J. Krüger, W. Kautek, and F. Krausz, "Incubation of laser ablation in fused silica with 5-fs pulses," Appl. Phys. A **69,** 465 (1999).

[13] A. Rosenfeld, M. Lorenz, R. Stoian, and D. Ashkenasi, "Ultrashort-laser-pulse damage threshold of transparent materials and the role of incubation," Appl. Phys. A **69,** S373 (1999).

[14] Z. Sun, M. Lenzner, and W. Rudolph, "Generic incubation law for laser damage and ablation thresholds," J. Appl. Phys. **117,** 073102 (2015).

[15] H. Sakurai, C. He, K. Konishi, H. Tamaru, J. Yumoto, M. Kuwata-Gonokami and A. Gillner, "Effect of damage incubation in the laser grooving of sapphire," J. Appl. Phys. **125,** 173109 (2019).

[16] J. F. Young, J. E. Sipe, and H. M. van Driel, "Laser-induced periodic surface structure. III. Fluence regimes, the role of feedback, and details of the induced topography in germanium," Phys. Rev. B **30,** 2001 (1984).

[17] D. Ashkenasi, A. Rosenfeld, H. Varel, M. Wahmer, and E. E. B. Campbell, "Subwavelength ripple formation on the surfaces of compound semiconductors irradiated with femtosecond laser pulses," Appl. Surf. Sci. **120,** 65 (1997).

[18] S. Sakabe, M. Hashida, S. Tokita, S. Namba, and K. Okamuro, "Mechanism for self-formation of periodic grating structures on a metal surface by a femtosecond laser pulse," Phys. Rev. B **79,** 033409-1 (2009).

[19] J. Bonse, J. Krüger, S. Höhm and A. Rosenfeld, "Femtosecond laser-induced periodic surface structures," J. Laser Appl. **24,** 4 (2012).

[20] M. Wuttig, N. Yamada, "Phase-change materials for rewriteable data storage," Nat. Mater. **6,** 824 (2007).

[21] P. K. Khulbe, X. Xun, and M. Mansuripur, "Crystallization and amorphization studies of a $Ge_2Sb_{2.3}Te_5$ thin-film sample under pulsed laser irradiation," Appl. Opt. **39,** 2359 (2000).

[22] S. Caravati, M. Bernasconi, T. D. Kühne, M. Krack, & M. Parrinello, "First-principles study of crystalline and amorphous $Ge_2Sb_2Te_5$ and the effects of stoichiometric defects," J. Phys. Condens. Matter **21,** 255501 (2009).

[23] G. Zhang, F. Gan, S. Lysenko, and H. Liu, "Observation of ultrafast carrier dynamics in amorphous Ge2Sb2Te5 films induced by femtosecond laser pulses," J. Appl. Phys. **101,** 033127 (2007).

[24] N. Yasumaru, K. Miyazaki, and J. Kiuchi, “Control of tribological properties of diamond-like carbon films with femtosecond-laser-induced nanostructuring,” Appl. Surf. Sci. **254,** 2364 (2008).

[25] R. A. Barb, C. Hrelescu, L. Dong, J. Heitz, J. Siegel, P. Slepicka, V. Vosmanska, V. Svorcik, B. Magnus, R. Marksteiner, M. Schernthaner, and K. Groschner, “Laser-induced periodic surface structures on polymers for formation of gold nanowires and activation of human cells,” Appl. Phys. A Mater. Sci. Process. **117,** 295 (2014).

[26] T. Shinonaga, M. Tsukamoto, A. Nagai, K. Yamashita, T. Hanawa, N. Matsushita, G. Xie, and N. Abe, “Cell spreading on titanium dioxide film formed and modified with aerosol beam and femtosecond laser,” Appl. Surf. Sci. **288,** 649 (2014).

[27] Q. Wu, Y. Ma, R. Fang, Y. Liao, Q. Yu, X. Chen, and K. Wang, “Femtosecond laser-induced periodic surface structure on diamond film,” Appl. Phys. Lett. **82,** 1703–1705 (2003).

[28] J. Bonse, S. Hohm, S. V. Kirner, A. Rosenfeld, and J. Kruger, “Laser-induced periodic surface structures- a scientific evergreen,” IEEE J. Sel. Top. Quantum Electron. **23**, 3 (2017).

[29] J. Bonse, A. Rosenfeld, and J. Krüger, “On the role of surface plasmon polaritons in the formation of laser-induced periodic surface structures upon irradiation of silicon by femtosecond-laser pulses,” J. Appl. Phys. **106,** 104910, (2009).

[30] G. Miyaji and K. Miyazaki, “Origin of periodicity in nanostructuring on thin film surfaces ablated with femtosecond laser pulses,” Opt. Express, **16,** 16265 (2008).

[31] F. Garrelie, J. P. Colombier, F. Pigeon, S. Tonchev, N. Faure, M. Bounhalli, S. Reynaud, and O. Parriaux, “Evidence of surface plasmon resonance in ultrafast laser-induced ripples,” Opt. Express, 19, 9035 (2011).

[32] T. Tomitaa, Y. Fukumori, K. Kinoshita, S. Matsuo, and S. Hashimoto, “Observation of laser-induced surface waves on flat silicon surface,” Appl. Phys. Lett. **92,** 013104 (2008).

[33] M. Kuwahara, O. Suzuki, Y. Yamakawa, N. Taketoshi, T. Yagi, P. Fons, T. Fukaya, J. Tominaga, and T. Baba, “Temperature dependence of the thermal properties of optical memory materials,” Jpn. J. Appl. Phys. **46,**

3909 (2007).

[34] M. Wuttig, H. Bhaskaran, and T. Taubner, “Phase-change materials for non-volatile photonic applications,” Nat. Photonics **11,** 465 (2017).

[35] X. Wang, M. Kuwahara, K. Awazu, P. Fons, J. Tominaga, and Y. Ohki, “Proposal of a grating-based optical reflection switch using phase change materials,” Opt. Express **17,** 16947 (2009).

[36] N. Yamada and T. Matsunaga, “Structure of laser-crystallized $Ge_2Sb_{2+x}Te_5$ sputtered thin films for use in optical memory,” J. Appl. Phys. **88,** 7020 (2000).

[37] T. Ohta, K. Yoshioka, H. Isomura, T. Akiyama, and R. Imanaka, “High-sensitivity overwritable phase-change optical disk for PD systems”, Proc. SPIE **2514,** 302 (1995).

[38] M. J. Shu, P. Zalden, F. Chen, B. Weems, I. Chatzakis, F. Xiong, R. Jeyasingh, M. C. Hoffmann, E. Pop, H. S. Philip Wong, M. Wuttig, and A.M. Lindenberg, “Ultrafast terahertz-induced response of GeSbTe phase-change materials,” Appl. Phys. Lett. **104,** 251907 (2014).

[39] M. Konishi, H. Santo, Y. Hongo, K. Tajima, M. Hosoi, T. Saiki, “Ultrafast amorphization in $Ge_{10}Sb_2Te_{13}$ thin film induced by single femtosecond laser pulse,” Appl. Opt. **49,** 18, 3470 (2010).

[40] T. Suzuki, R. Hida, Y. Yamaguchi, K. Nakagawa, T. Saiki, and F. Kannari, “Single-shot 25-frame burst imaging of ultrafast phase transition of $Ge_2Sb_2Te_5$ with a sub-picosecond resolution,” Appl. Phys. Express **10,** 092502 (2017).

[41] A. V. Kolobov, P. Fons, A. I. Frenkel, A. L. Ankudinov, J. Tominaga, and T. Uruga, “Understanding the phase-change mechanism of rewritable optical media,” Nat. Mater. **3,** 703 (2004).

[42] A. V. Kolobov, A. S. Mishchenko, P. Fons, S. M. Yabubenya, and J. Tominaga, “A possible mechanism of ultrafast amorphization in phase-change memory alloys: an ion slingshot from the crystalline to amorphous position,” J. Phys. Condens. Mat. **19,** 455209 (2007).

[43] X-B. Li, X. Q. Liu, X. Liu, D. Han, Z. Zhang, X. D. Han, H-B. Sun, and S. B. Zhang, “Role of electronic excitation in the amorphization of Ge-Sb-Te alloys,” Phys. Rev. Lett. **107,** 015501 (2011).

[44] K. Makino, K. Kato, K. Takano, Y. Saito, J. Tominaga, T. Nakano, G. Isoyama, and M. Nakajima, “Significant volume expansion as a

precursor to ablation and micropattern formation in phase change material induced by intense terahertz pulses," Sci. Rep. **8,** 2914 (2018).

[45] S. Kozyukhin, P. Lazarenko, Y. Vorobyov, A. Baranchikov, V. Glukhenkaya, M. Smayev, A. Sherchenkov, Y. Sybina, A. Polohin, and V. Sigaev, "Laser-induced modification and formation of periodic surface structures (ripples) of amorphous GST225 phase change materials," Opt. Laser Technol. **113,** 87 (2019).

[46] J. Takeda, W. Oba, Y. Minami, T. Saiki, and I. Katayama, "Ultrafast crystalline-to-amorphous phase transition in $Ge_2Sb_2Te_5$ chalcogenide alloy thin film using single-shot imaging spectroscopy," Appl. Phys. Lett. **104,** 261903 (2014).

[47] I. A. Shkrob, D. A. Oulianov, R. A. Crowell, and S. Pommeret, "Frequency-domain "single-shot" ultrafast transient absorption spectroscopy using chirped laser pulses," J. Appl. Phys. **96,** 25 (2004).

[48] H. Hirori, K. Shinokita, M. Shirai, S. Tani, Y. Kadoya and K. Tanaka, "Extraordinary carrier multiplication gated by a picosecond electric field pulse," Nat. Commun. **2,** 594 (2011).

Chapter 5

Chapter 6

Conclusion and Outlook

In this thesis, we have demonstrated a high-repetition-rate single-shot measurement system [1,2] that combines the chirped-pulse single-shot method [3-5] with the photonic time-stretch method [6-9].

In Chapter 3, we demonstrated the concept of a high-repetition-rate single-shot measurement system using a long optical fiber and oscilloscope [1]. To verify the feasibility of high-repetition measurements, we demonstrated Kerr gate measurements in LiNbO3 crystals using a Ti:Sapphire CPA laser at 1-kHz repetition. As a result, we obtained the pump intensity dependence of optical Kerr signals within one second.

In Chapter 4, to acquire single-shot pump-probe waveforms for each laser pulse at a high-repetition-rate with good signal-to-noise ratio and to improve the variability of the time window, we introduced a CFBG and a grating pair pulse stretcher to our high-repetition-rate single-shot measurement system [2]. Using a CFBG, the signal-to-noise ratio of probe pulses was dramatically improved compared with the case using a long optical fiber. The variable time window of the measurement was demonstrated using a grating pair, which allowed us to extend observable phenomena and materials.

Finally, in Chapter 5, using high-repetition-rate single-shot spectroscopy and microscopic images taken by a laser microscope, we demonstrated the observation of pulse-to-pulse dynamics from initial photoexcitation to LIPSS formation via the crystalline-to-amorphous phase change in GST thin films. Above the threshold excitation density for LIPSS formation, the first excitation pulse induces photoinduced amorphization in the picosecond timescale and subsequent pulses gradually form LIPSS on the amorphous phase. During the latter process, the amplitude and relaxation time of the transient transmittance gradually decrease, indicating accelerated relaxation of the excitation energy, which causes structural deformation.

Our method is a novel modification of a serial time-encoded amplified microscopy (STEAM) camera for imaging, or the previously reported time-stretch dispersive Fourier transformation method [9,10]. In this work, we used a similar dispersive optic to stretch the temporal information from femtosecond or picosecond to nanosecond timescales, rather than using Fourier transformation. Although the basic principle has been previously proposed for picosecond to nanosecond time-stretch [11], our experimental demonstrations pave the way for remarkable capabilities in ultrafast measurements of irreversible phenomena, such as photoinduced phase changes and LIPSS formation. These results could contribute to understanding the fundamental mechanisms of laser processing in terms of the observation of pulse-to-pulse dynamics.

Additionally, the observation of ultrafast dynamics at each pulse is important in many fields, such as laser chaos [12-14], optical solitons [15-17], biotechnology, and laser processing. Using our method, pulse-by-pulse accumulation effects, such as incubation effects [18-21], can be observed at the same time as processing, without removing the sample from the fabrication table. Combined with high-speed imaging techniques, this will make a significant contribution to understanding the irreversible dynamics and to industrial applications, especially in laser processing. Furthermore, most of the studies using the photonic time-stretch method, including this study, have been conducted in the visible or NIR wavelength range. If this method can be applied to the infrared wavelength range, it will also be possible to study protein folding dynamics [22-25], phase change dynamics, laser processing of organic materials using high-intensity lasers [26,27], and photodegradation of organic solar cell materials [28-30]. Such dynamics are nearly unexplored and our demonstrated improvements can open a new frontier for ultrafast dynamics research and applications.

References

[1] M. Kobayashi, Y. Minami, C. L. Johnson, P. D. Salmans, N. R. Ellsworth, J. Takeda, J. A. Johnson and I. Katayama, “High-acquisition-rate single-shot pump-probe measurements using time-stretching method,” Sci. Rep. **6,** 37614 (2016).

[2] M. Kobayashi, Y. Arashida, G. Yamashita, E. Matsubara, M. Ashida, J. A. Johnson, and I. Katayama, “Fast-frame single-shot pump-probe spectroscopy with chirped-fiber-Bragg gratings,” Opt. Lett. **44,** 163 (2019).

[3] K. Y. Kim, B. Yellampalle, G. Rodriguez, R. D. Averitt, A. J. Taylor, and J. H. Glownia, “Single-shot, interferometric, high-resolution, terahertz field diagnostic,” App. Phys. Lett. **88,** 041123 (2006).

[4] B. Yellampalle, K. Y. Kim, G. Rodriguez, J. H. Glownia, and A. J. Taylor, “Algorithm for high-resolution single-shot THz measurement using in-line spectral interferometry with chirped pulses,” App. Phys. Lett. **87,** 211109 (2005).

[5] J.-P. Geindre, P. Audebert, S. Rebibo, and J.-C. Gauthier, “Single-shot spectral interferometry with chirped pulses,” Opt. Lett. **26,** 1612 (2001).

[6] A. S. Bhushan, F. Coppinger, and B. Jalali, “Time-stretched analog-to-digital conversion,” Electron. Lett. **34,** 9, 839 (1998).

[7] F. Coppinger, A. S. Bhushan, and B. Jalali, “Time magnification of electrical signals using chirped optical pulses,” Electron. Lett. **34,** 4, 399 (1998).

[8] F. Coppinger, A. S. Bhushan, and B. Jalali, “Photonic time stretch and its application to analog-to-digital conversion,” IEEE Transactions on microwave theory and techniques **47,** 7 (1999).

[9] K. Goda, K. K. Tsia and B. Jalali, “Serial time-encoded amplified imaging for real-time observation of fast dynamic phenomena,” Nature **458,** 7242, 1145 (2009).

[10] K. Goda and B. Jalali, “Dispersive Fourier transformation for fast continuous single-shot measurements,” Nat. Photon. **7,** 102 (2013).

[11] S. Gupta and B. Jalali, “Time stretch enhanced recording oscilloscope,” Appl. Phys. Lett. **94,** 041105 (2009).

[12] T. Sugawara, M. Tachikawa, T. Tsukamoto and T. Shimizu, “Observation of synchronization in laser chaos,” Phys. Rev. Lett. **72,** 3502 (1994).

[13] S. Boccaletti, J. Kurths, G. Osipov, D. L. Valladares and C. S. Zhou, “The synchronization of chaotic systems,” Physics Reports **366,** 1 (2002).

[14] E. J. Doedel and C. L. Pando L., “Rare events in mixed-mode oscillations from weakly coupled lasers,” Phys. Rev. E **100,** 052204 (2019).

[15] J. R. Taylor, “Optical solitons,” Cambridge University Press, UK (1992).

[16] A. Hasegawa, “Optical solitons in fibers,” Springer, Berlin, Heidelberg (1989).

[17] C. Markos, J. C. Travers, A. Abdolvand, B. J. Eggleton, and O. Bang, “Hybrid photonic-crystal fiber,” Rev. Mod. Phys. **89,** 045003 (2017).

[18] M. Lenzner, J. Krüger, W. Kautek, and F. Krausz, “Incubation of laser ablation in fused silica with 5-fs pulses,” Appl. Phys. A **69**, 465 (1999).

[19] A. Rosenfeld, M. Lorenz, R. Stoian, and D. Ashkenasi, “Ultrashort-laser-pulse damage threshold of transparent materials and the role of incubation,” Appl. Phys. A **69**, S373 (1999).

[20] Z. Sun, M. Lenzner, and W. Rudolph, “Generic incubation law for laser damage and ablation thresholds,” J. Appl. Phys. **117**, 073102 (2015).

[21] H. Sakurai, C. He, K. Konishi, H. Tamaru, J. Yumoto, M. Kuwata-Gonokami and A. Gillner, “Effect of damage incubation in the laser grooving of sapphire,” J. Appl. Phys. **125**, 173109 (2019).

[22] H. S. Chan and K. A. Dill, “Transition states and folding dynamics of proteins and heteropolymers,” J. Chem. Phys. **100,** 9238 (1994).

[23] B. Alberts, A. Johnson, J. Lewis, M. Raff, K. Roberts and P. Walter, “Molecular biology of the cell, 4th edition,” Garland Science, New York (2002).

[24] D. E. Shaw, P. Maragakis, K. Lindorff-Larsen, S. Piana, R. O. Dror, M. P. Eastwood, J. A. Bank, J. M. Jumper, J. K. Salmon, Y. Shan and W. Wriggers, “Atomic-level characterization of the structural dynamics of proteins,” Science **330**, 6002, 341 (2010).

[25] C. D. Snow, H. Nguyen, V. S. Pande and M. Gruebele, "Absolute comparison of simulated and experimental protein-folding dynamics," Nature **420,** 102 (2002).

[26] D. Bäuerle, "Laser processing and chemistry," Springer Science & Business Media (2013).

[27] H. Haferkamp, F. von Alvensleben, D. Seebaum, M. Goede and T. Püster, "Air contaminants generated during laser processing of organic materials and protective measures," Journal of Laser Applications **10,** 109 (1998).

[28] Y. Yamada, T. Yamada, A. Shimazaki, A. Wakamiya and Y. Kanemitsu, "Interfacial charge-carrier trapping in $CH_3NH_3PbI_3$-based heterolayered structures revealed by time-resolved photoluminescence spectroscopy," J. Phys. Chem. Lett. **7,** 11 (2016).

[29] L. Wang, C. McCleese, A. Kovalsky, Y. Zhao and C. Burda, "Femtosecond time-resolved transient absorption spectroscopy of $CH_3NH_3PbI_3$ perovskite films: evidence for passivation effect of PbI_2," J. Am. Chem. Soc. **136,** 12205 (2014).

[30] K. Kawano and C. Adachi, "Evaluating carrier accumulation in degraded bulk heterojunction organic solar cells by a thermally stimulated current technique," Adv. Funct. Mater. **19**, 24, 3934 (2009).

Chapter 6

List of Publications

Publications from this Thesis

[1] Masataka Kobayashi, Yasuo Minami, Courtney L. Johnson, Parker D. Salmans, Nicholas R. Ellsworth, Jun Takeda, Jeremy A. Johnson, and Ikufumi Katayama, “High-Acquisition-Rate Single-Shot Pump-Probe Measurements Using Time-Stretching Method,” Sci. Rep. **6,** 37614 (2016).

[2] Masataka Kobayashi, Yusuke Arashida, Genki Yamashita, Eiichi Matsubara, Masaaki Ashida, Jeremy A. Johnson, and Ikufumi Katayama, “Fast-Frame Single-shot Pump-Probe Spectroscopy with Chirped-Fiber-Bragg Gratings,” Opt. Lett. **44,** 163-166 (2019).

[3] Masataka Kobayashi, Yusuke Arashida, Kanta Asakawa, Keisuke Kaneshima, Masashi Kuwahara, Kuniaki Konishi, Junji Yumoto, Makoto Kuwata-Gonokami, Jun Takeda, and Ikufumi Katayama, “Pulse-to-pulse Ultrafast Dynamics of Highly Photoexcited $Ge_2Sb_2Te_5$ Thin Films,” Under Construction.

Presentations at Conferences

International Conferences

[1] M. Kobayashi, Y. Minami, C. L. Johnson, P. D. Salmans, N. R. Ellsworth, J. Takeda, J. A. Johnson, and I. Katayama, "Fast-Frame Single-Shot Acquisition of Ultrafast Waveforms," *International Conference on Ultrafast Phenomena 2016*, UTh4A.28, Santa Fe, New Mexico, USA, July 2016. (Poster Presentation)

[2] I. Katayama, M. Kobayashi, Y. Minami, J. Takeda, C. L. Johnson, P. D. Salmans, N. R. Ellsworth, and J. A. Johnson, "Single-shot Terahertz Detection Using a GHz Bandwidth Oscilloscope," *41st International Conference on Infrared, Millimeter and Terahertz Waves* (IRMMW-THz 2016), M4B.4, Copenhagen, Denmark, September 2016. (Oral Presentation)

[3] M. Kobayashi, Y. Arashida, Y. Minami, J. Takeda, J. A. Johnson, and I. Katayama, "High-Repetition-Rate Single-Shot Spectroscopy of Photoinduced Phase-Change Materials," *The 24th Congress of the International Commission for Optics* (ICO-24), Th3D-05, Tokyo, Japan, August 2017. (Oral Presentation)

[4] M. Kobayashi, Y. Arashida, G. Yamashita, E. Matsubara, M. Ashida, J. A. Johnson, and I. Katayama, "High-acquisition-rate single-shot pump-probe measurement using chirped-fiber Bragg gratings," *CLEO/Europe-EQEC 2019*, CF-P.2, Munich, Germany, June 2019. (Poster Presentation)

[5] M. Kobayashi, Y. Arashida, K. Asakawa, K. Konishi, J. Yumoto, M. Kuwata-Gonokami, J. Takeda, and I. Katayama, "Ultrafast Dynamics in $Ge_2Sb_2Te_5$ Thin Films during Laser-Induced Successive Surface Modification," *International Conference on Ultrafast Phenomena 2020*, M4A.23, November 2020. (Online Poster Presentation)

Domestic Conferences

■ Oral Presentation

[1] M. Kobayashi, J. A. Johnson, Y. Minami, J. Takeda, and I. Katayama, "High speed Single shot Detection of Terahertz Electric Field Waveform," *The 62th JSAP Spring Meeting*, 13p-A14-9, Tokai Univ., March 2015.

[2] M. Kobayashi, J. A. Johnson, Y. Minami, J. Takeda, and I. Katayama, "Single-shot Detection of Terahertz Waveform using Chirped Pulses," *Optics & Photonics Japan 2015*, 29aC9, Univ. of Tsukuba, October 2015.

[3] M. Kobayashi, J. A. Johnson, Y. Minami, J. Takeda, and I. Katayama, "High-repetition Single-shot Detection of Ultrafast Photoinduced Phenomena," *The 77th JSAP Autumn Meeting*, 14p-C32-4, Toki Messe, September 2016.

[4] M. Kobayashi, J. A. Johnson, Y. Minami, J. Takeda, and I. Katayama, "High-Repetition-Rate Single-Shot Spectroscopy of Phot-induced Phase-Change Materials," *Optics & Photonics Japan 2016*, 2aB7, Univ. of Tsukuba, November 2016.

[5] M. Kobayashi, J. A. Johnson, Y. Arashida, Y. Minami, J. Takeda, G. Yamashita, M. Ashida, and I. Katayama, "Fiber Based Single Shot Spectroscopy with Chirped Fiber Bragg Grating," *The 64th JSAP Spring Meeting*, 16p-311-13, PACIFICO Yokohama, March 2017.

[6] M. Kobayashi, Y. Arashida, J. Takeda, and I. Katayama, "Simultaneous Measurement of Carrier Generation and Long-Lived Relaxation of Si using High Repetition-rate Single-Shot Spectroscopy," *The 79th JSAP Autumn Meeting*, 21p-211A-12, Nagoya Congress Center, September 2018.

[7] M. Kobayashi, Y. Arashida, J. Takeda, and I. Katayama, "Simultaneous Measurement of Carrier Generation and Long-Lived Relaxation of Si using High Repetition-rate Single-Shot Spectroscopy," *The 8th Workshop on Hybrid Quantum Systems*, Okinawa Institute of Science and Technology Graduate University (OIST), January 2019.

[8] M. Kobayashi, Y. Arashida, J. Takeda, and I. Katayama, "Multi Time scale Measurement of Photoexcited Carriers in Si using High Repetition rate Single Shot Spectroscopy," *The 39th Annual Meeting of Laser Society of Japan*, F212pX06, Tokai Univ., January 2019.

[9] M. Kobayashi, K. Asakawa, Y. Arashida, K. Konishi, J. Yumoto, M. Kuwata-Gonokami, J. Takeda, and I. Katayama, "Observation of Ultrafast Dynamics Associated with Multi-Shot LIPPS Formation in $Ge_2Sb_2Te_5$ Thin Films Using High Repetition-Rate Single-Shot Spectroscopy," *The 80th JSAP Autumn Meeting*, 19p-E205-6, Hokkaido Univ., September 2019.

[10] M. Kobayashi, K. Asakawa, Y. Arashida, K. Konishi, J. Yumoto, M. Kuwata-Gonokami, J. Takeda, and I. Katayama, "Ultrafast Dynamics of LIPSS Formation in $Ge_2Sb_2Te_5$ Thin Films Using High Repetition-Rate Single-Shot Spectroscopy," *The 67th JSAP Spring Meeting*, 13p-B410-7, Sophia Univ., March 2020.

■ Poster Presentation

[1] M. Kobayashi, J. A. Johnson, Y. Minami, J. Takeda, and I. Katayama, "High speed Single shot Detection of Terahertz Electric Field Waveform with Optical Fiber," *The 10th Nanotech Communication Symposium*, N-45, Yokohama City Univ., March 2015.

[2] M. Kobayashi, J. A. Johnson, Y. Minami, C. L. Johnson, P. D. Salmans, N. R. Ellsworth, J. Takeda, and I. Katayama, "Development of a Terahertz Oscilloscope using a fiber based scheme with chirped pulses," *The 11th Nanotech Communication Symposium*, N-68, Yokohama National Univ.,

March 2016.

[3] M. Kobayashi, J. A. Johnson, Y. Arashida, Y. Minami, J. Takeda, and I. Katayama, “High repetition Single shot Spectroscopy of Ultrafast Photoinduced Phenomena,” *The 12th Nanotech Communication Symposium*, N-8, Yokohama City Univ., March 2017.

[4] M. Kobayashi, “High-Repetition-Rate Single-Shot Spectroscopy of Photoinduced Phase-Change Materials,” *The 24th Laser Summer School*, B-19, NTT Hokkaido Seminar Center, October 2017.

[5] M. Kobayashi, Y. Arashida, G. Yamashita, E. Matsubara, M. Ashida, J. A. Johnson, J. Takeda, and I. Katayama, “High-acquisition-rate single-shot pump-probe measurement using chirped-fiber Bragg gratings,” *The 9th Workshop on Hybrid Quantum Systems*, P07, Japan Advanced Institute of Science and Technology (JAIST), August 2019.

[6] M. Kobayashi, “Observation of Ultrafast Dynamics Associated with Multi-Shot LIPSS Formation in $Ge_2Sb_2Te_5$ Thin Films Using High Repetition-Rate Single-Shot Spectroscopy” *The 26th Laser Summer School*, A-1, FORUM246, October 2019.

[7] M. Kobayashi, K. Asakawa, Y. Arashida, K. Konishi, J. Yumoto, M. Kuwata-Gonokami, J. Takeda, and I. Katayama, “Multi-timescale Dynamics Associated with Multi-Shot LIPSS Formation in $Ge_2Sb_2Te_5$ Thin Films,” *The 4th JSAP Photonics Workshop*, PW-1P, Okinawaken Seinenkaikan, November 2019.

[8] M. Kobayashi, K. Asakawa, Y. Arashida, K. Konishi, J. Yumoto, M. Kuwata-Gonokami, J. Takeda, and I. Katayama, “Visualization of Ultrafast Dynamics and Multi-Shot LIPSS Formation in $Ge_2Sb_2Te_5$ Thin Films,” *The 30th Association for Condensed Matter Photophysics*, II-61, Kyoto Univ., December 2019.

Presentations at conferences

Appendix A

Radio Frequency Controller of the Acousto-Optic Modulator

In Chapter 5, an acousto-optic modulator (AOM) was introduced into our experimental setup to reduce the repetition of the pump pulse. Before using the system, a radio frequency (RF) controller was made to control the AOM. In this appendix, the principle of the AOM system and the design of the RF controller is briefly explained.

First, the interaction of sound and light, so-called acousto-optics, was predicted by Brillouin in 1922 [1] and experimentally confirmed in 1932 [2,3]. Acousto-optic devices are now widely used in many fields to control of polarization and modulation of laser light. The development history and theory of acousto-optics are reviewed in detail in Ref. [4] and [5]. Figure A1 shows a schematic of the Bragg diffraction cell used as an AOM. A periodic refractive index change is produced when a RF signal is applied to an acousto-optic element. AOM uses this effect as a diffraction grating and outputs first-order diffracted light. By controlling the duration of the applied RF signal, we can adjust the time width of the diffracted light and, especially in the case of a pulsed laser light source, it becomes possible to control the repetition rate of the pulses.

In our experiment in Chapter 5, we used an AOM with TeO_2 as the acousto-optic medium (Gooch & Housego, 3080-197), in which the operational RF and light wavelength range are 80 MHz and 1047-1060 nm, respectively. To control the AOM, we made a RF controller, as shown in Figure A2. The voltage-controlled oscillator

Appendix A

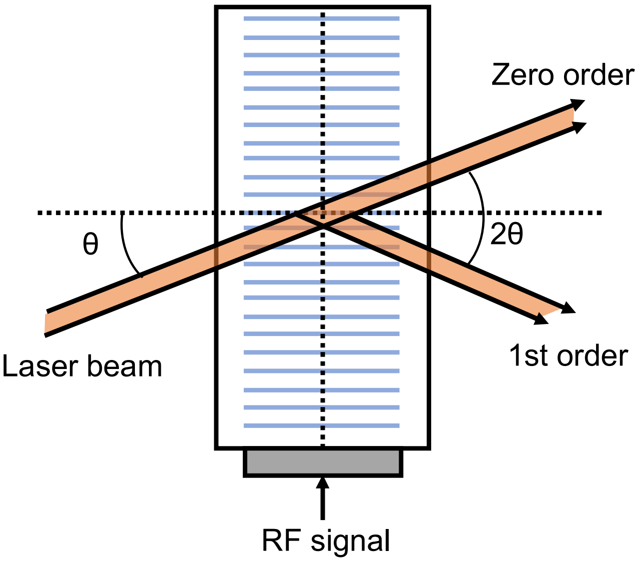

Figure A.1 | Schematic of a Bragg diffraction sound cell used as a modulator.

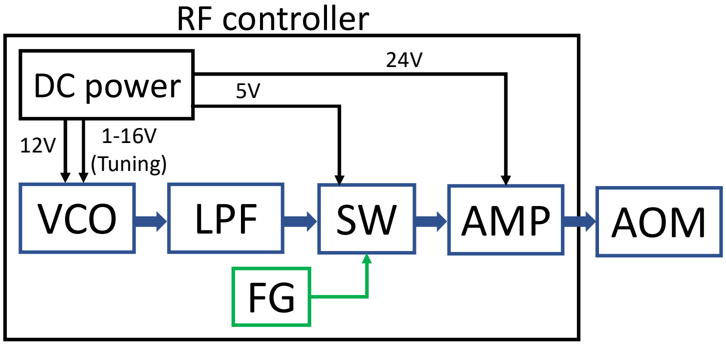

Figure A.2 | Schematic of an RF controller. VCO: voltage-controlled oscillator, LPF: Low pass filter, SW: High isolation switch, AMP: amplifier, AOM: acousto-optic modulator, FG: function generator.

(VCO, Mini-Circuits POS-100+) could oscillate a RF signal with a frequency between 50 - 100 MHz and, by adjusting the applied tuning voltage, the oscillated radio frequency was set to 80 MHz. Then, the high-frequency component in the oscillated signal was removed by a low pass filter (LPF, Mini-Circuits RLP-105+). The signal from the LPF could be switched by a high isolation switch (Mini-Circuits ZASWA-2-50DR+). The timing of the RF signal output was controlled by a function generator (FG, TEXIO FGX-2220). Finally, the RF signal was amplified to 1 W and induced to the AOM.

References

[1] L. Brillouin, "Diffusion de la lumière et des rayons X par un corps transparent homogène," Ann. Phys. (Paris) **17**, 88 (1922).

[2] R. Lucas and P. Biquard, "Propriétés optiques des milieux solides et liquides soumis aux vibration élastiques ultra sonores," J. Phys. Rad. **3,** 464 (1932).

[3] P. Debye and F. W. Sears, "On the scattering of light by supersonic waves," Proc. Nat. Acad. Sci. (U.S.) **18,** 409 (1932)

[4] E. I. Gordon, "A review of acoustooptical deflection and modulation devices," Appl. Opt. **5,** 10, 1629 (1966).

[5] A. Korpel, "Acousto-optics -A review of fundamentals," Proc. IEEE **69**, 48 (1981).

Appendix A

Appendix B

Data Acquisition System using FastFrame® Mode

In this thesis, thousands of single-shot waveforms were acquired within a few seconds in one measurement using a high-repetition-rate single-shot system. Particularly, we used the FastFrame® (FF) mode of the real-time oscilloscope (Tektronix DPO71244C) to acquire single-shot waveforms, such as those shown in Figure 4.10 in Chapter 4 and Figure 5.8 in Chapter 5. The FF mode acquires short burst signals and stores them as frames for detailed observation and analysis. Depending on the memory capacity of the oscilloscope and time resolution of the waveform, we can acquire thousands of frames. In this appendix, we explain the flow of the acquisition of single-shot waveforms using FF mode and the analysis program.

Figure B.1 shows the flowchart of the FF mode for acquiring 2,000 single-shot waveforms. When the FF mode is activated and the oscilloscope is set to acquire 2,000 waveforms in the mode, the oscilloscope waits to acquire the waveforms until the trigger signal is input. Once a trigger signal is input, the oscilloscope acquires a signal waveform and increases the waveform counter by one. The oscilloscope repeatedly acquires and stores single-shot waveforms in temporary memory, each time the trigger signal is input, until the waveform counter reaches 2,000. Finally, the oscilloscope saves the 2,000 single-shot waveforms as a dataset WFM file into an internal hard-disk drive. Considering these operational features of the FF mode, a delay generator was used to control the timing of the trigger signal input into the

Appendix B

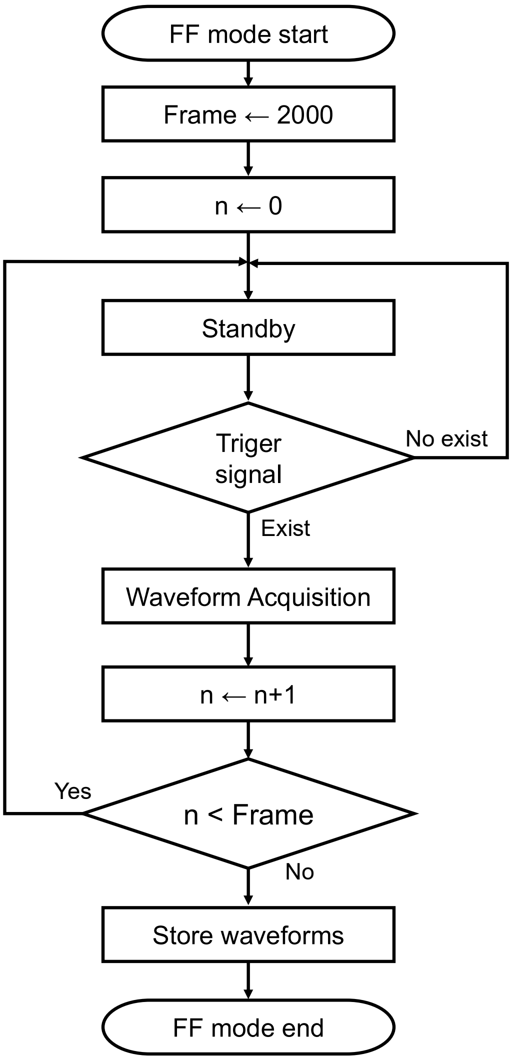

Figure B.1 | Flowchart of the FF mode in the real-time oscilloscope.

oscilloscope to synchronize the timing of the pump pulse irradiation on the GST sample with the timing of the single-shot waveform acquisition in Chapter 5.

After acquisition of the WFM files with pump and probe waveforms, we normalized the waveforms and obtained pump-probe traces using data analysis software, Igor Pro 8 version 8.04 (WaveMetrics). Table B.1 shows the sample macro code used to normalize pump-probe traces from WFM files in Igor Pro 8. In the macro, the WFM files containing pump waveforms are first loaded and the peak intensity for each frame is assigned to the 1D waveform data, named “Pumpinfo.” Second, the WFM files contained probe waveforms are loaded and converted from

Table B.1 | Sample macro code to normalize pump-probe traces from WFM files in Igor Pro 8 ver. 8.04.

```
Macro Normalization (PN,FN,del_time,RS,RE,timescale,str)
   variable PN = 1032, FN = 2000, del_time = 0.01, RS = 300, RE = 700
   String timescale,str
   prompt timescale,"Timescale wave",popup,WaveList("*",";","")

   variable iii = PN          //Number of points per waveform.
   variable jjj = FN          //Total number of frames.
   variable www = 0           //Number of graphs displayed.

Silent 1
PauseUpdate

//Loading Waveforms.
   GBLoadWave/T={8,4}/S=108784/W=1/N=PumpFrame           //Load pump pulse waveforms.
   Redimension/N=(iii,jjj) PumpFrame0                    //Conversion from 1D data to 2D matrix.
   WaveStats/Q PumpFrame0                                //Minimum value detection.
   PumpFrame0 = PumpFrame0+abs(V_min)                    //Offsetting.

   Make/O/N=(DimSize(PumpFrame0,1))/D Pumpinfo
   Pumpinfo = PumpFrame0[V_maxRowLoc][p]                 //Detect the peak intensity for each frame.
   Duplicate/O   Pumpinfo   $(str+"_PumpInfo")           //Change the data name.

   GBLoadWave/T={8,4}/S=108784/W=1/N=FF       //Load probe pulse waveforms.
   Redimension/N=(iii,jjj) FF0                //Conversion from 1D data to 2D matrix.
   WaveStats/Q FF0                            //Minimum value detection.
   FF0 = FF0+abs(V_min)                       //Offsetting.

   SetScale/I x 0,iii*del_time, FF0       //Convert the horizontal axis to nanoseconds.
   Duplicate/O/R=[RS,RE]   FF0   $(str+"_MImage")
                                          //Change the waveform name and delete extra data points.

//Normalize the signal waveforms
   Duplicate/O FF0 NormImage              // Make a 2D matrix to assign normalized waveforms.
   Duplicate/O FF0 ReflImage              // Make a 2D matrix to assign reference waveforms.

   Wavestats/Q Pumpinfo                   //Detect the maximum value of pump power.
   variable PumpMax = V_max               //Assign the maximum power of the pump.
   variable nn = 0                        //Frame count.
   variable NromN = 0                     //Count the number of normalized waveforms generated.

   do
       if(PumpInfo[nn] > (PumpMax*0.5))
          NormImage[][NromN]=(FF0[p][nn]-((FF0[p][nn+1]+FF0[p][nn-1])/2))/((FF0[p][nn+1]+FF0[p][nn-1])/2)
          NromN+=1
       endif
       nn+=1
   while(nn < DimSize(FF0,1))


// Convert the horizontal axis of the normalized waveform to picosecond scale.
   Duplicate/O $timescale timescale2
   SetScale/I x timescale2[0],timescale2[(DimSize(timescale2,0))-1], NormImage

   Duplicate/O/R=[RS,RE]   NormImage   $(str+"_Norm_pico")
                                             //Change the waveform name and delete extra data points.
   Display/W=(0+250*www,0,250+250*www,200);AppendImage $(str+"_Norm_pico")      //Display graph.

//Modify the appearance of the graph.
   ModifyImage $(str+"_Norm_pico") ctab= {-1,1,Rainbow,1}
   ModifyGraph font="Times New Roman", fsize=16, manTick=0, tick=2
   ModifyGraph tick(bottom)=2, axThick(bottom)=1, axThick=1, standoff=1
   ModifyGraph highTrip(left)=10000, mirror(bottom)=2, mirror=2
   ModifyGraph margin=0, tick=0, minor=1, btLen=5
   Label left "¥Z16Pump Shot Number"
   Label bottom "¥Z16Time (ps)"

end
```

1D data to a 2D matrix named “FF0.” Third, by referring to “Pumpinfo,” the probe waveforms in the frame, which were irradiated by the pump pulse, are read out from the 2D Matrix “FF0.” Then, the probe waveforms are normalized, by the averages of the frames before and after, as reference waveforms. Finally, converting the horizontal axis of the normalized waveforms to the picosecond timescale, we obtain normalized pump-probe traces.

Appendix C

Ablation of $Ge_2Sb_2Te_5$

In this appendix, supplementary information of the ablation of GST, which was not included in Chapter 5, is provided. Figure C.1(a) and (b) show microscopic surface images of GST films after irradiation with 400 pulses at 33 and 42 mJ/cm2 pump fluences, respectively. Red dashed circles indicate the irradiation location with 30-μm-diameter probe pulses. Corresponding pump-probe traces as a function of the pump laser shot were plotted in a 2D image, as shown in Figs. C.1(c) and (d). As can be clearly seen in Figure C.1(a) and (b), the black area in the center of the microscopic images is the ablation region of GST, wherein the sapphire substrate is

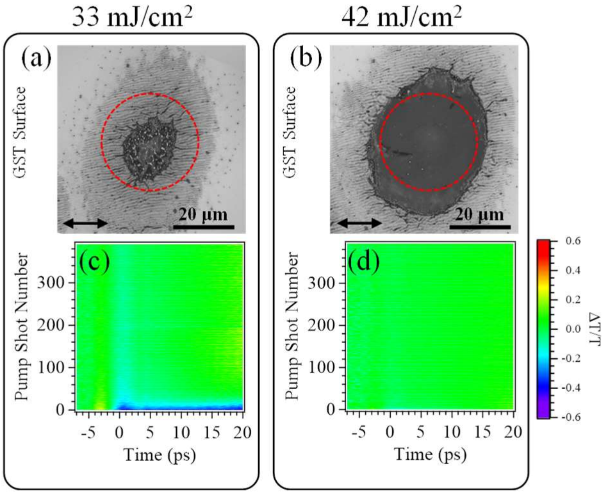

Figure C.1 | (a), (b) Microscopic images of GST after irradiation with 400 pulses at 33 and 42 mJ/cm^2 pump fluences. Arrows indicate the polarizations of the pump pulses. (c), (d) The pump-probe ultrafast traces for each pump laser shot plotted in a 2D color image. The vertical axis is the number of pump laser shots and the horizontal axis is the pump-probe delay time.

exposed. At the periphery of the ablation, LIPSS was formed parallel to the polarization of the pump pulse, which is the same as that described in Chapter 5.

In this ablation region, only a few pulses of the pump-probe waveform were obtained at 33 mJ/cm2, as shown in Fig. C.1(c), since the sapphire substrate was revealed in the majority of the probe pulse irradiation area. However, in the case of a 42 mJ/cm2 pump fluence, shown in Fig. C.1(d), we could not get the waveform because the entire probe pulse irradiation area was ablated.